

Emil Solbakken

NTNU
Norwegian University of
Science and Technology
Faculty of Engineering
Department of Geoscience and Petroleum

Emil Solbakken

Snow surface mapping and change detection in avalanche release areas using a consumer-grade UAS and SfM photogrammetry

September 2019





Norwegian University of
Science and Technology

Snow surface mapping and change detection in avalanche release areas using a consumer-grade UAS and SfM photogrammetry

Emil Solbakken

Master's thesis in Geology

Submission date: September 2019

Supervisor: Bjørn Frengstad, IGP

Co-supervisor: Tore Humstad, NPRA

Norwegian University of Science and Technology
Department of Geoscience and Petroleum

Abstract

The use of unmanned aerial systems (UASs) and Structure-from-Motion (SfM) photogrammetry for topographic mapping of snow surfaces has gained increased attention in recent years. High ground resolution, low cost and large flexibility make the method relevant for many purposes, including operational avalanche hazard evaluation. One potential application is monitoring of snow accumulation in avalanche release areas, which could be valuable for assessing the hazard from dry-snow slab avalanches. Surveying in avalanche terrain is however challenged by limited access, which in turn is limiting the options for placing ground control points and check points to be used for georeferencing and error assessment. In addition, as previous studies have pointed out, even snow surfaces represent a difficult task for the automatic feature detection and matching inherent in SfM processing.

In this study, digital elevation models (DEMs) of 0.1 m resolution and sub-decimetre accuracy were obtained from repeated surveys of an avalanche release area at Tyinstølen, Norway. By implementing detailed analyses of errors and sensitivity of parameters throughout the photogrammetric processing, uncertainties in the final DEMs and possible causes could be identified. Snow surface change between surveys was then quantified by calculation of DEMs of difference, and uniform levels of detection (LoDs) were applied to evaluate the significance of detected changes. Changes were also qualitatively evaluated on the basis of weather observations from the given time periods.

The results show that snow depth changes of minimum 10-20 cm were reliably detected, but also that survey precision was limited by both methodical and systematical aspects. Weak image geometry, with subsequent poor camera calibration, was together with the distribution of ground control points sources of considerable spatial variability in DEM precision.

Sammendrag

Topografisk kartlegging av snøoverflater med drone og Structure-from-Motion (SfM) fotogrammetri er en relativt ny metode som har fått økt oppmerksomhet de siste årene. Høy oppløsning av terrengmodeller, lave kostnader og stor fleksibilitet gjør metoden aktuell til mange formål, blant annet innen vurdering av snøskredfare. En mulig anvendelse er overvåkning av snødybde i løsnemråder for snøskred, noe som kan være særlig nyttig for vurdering av faren for tørre flakskred. Kartlegging i skredterreng er imidlertid generelt krevende, da begrensede muligheter for adkomst snevrer inn mulighetene for utplassering av kontrollpunkter for georeferering og validering av terrengmodellen. Dessuten har tidligere studier påpekt at jevne snøoverflater med lite kontraster er et vanskelig utgangspunkt for automatisk bildegjenkjenning og -matching, som er en grunnleggende del av SfM-prosesseringen.

Studien omfattet etablering av digitale høydemodeller (DEM-er) med 0,1 m oppløsning og nøyaktighet mellom 5 og 10 cm fra gjentatte innmålinger av et løsnemråde for snøskred ved Tyinstølen i Norge. Inngående analyser av feilkilder og sensitivitet til parametere underveis i prosesseringen gjorde det mulig å vurdere gjenværende usikkerhet i ferdige terrengmodeller og avdekke sannsynlige årsaker til denne. Endring i snødybde mellom innmålingene ble så regnet ut og vurdert for statistisk signifikans ved hjelp av deteksjonsgrenser basert på nøyaktigheten til hver enkelt modell. Endringene ble også kvalitativt vurdert med bakgrunn i værdata fra de aktuelle periodene.

Resultatene viser at endringer i snødybde på minimum 10-20 cm ble detektert med stor grad av sikkerhet, men også at oppnådd nøyaktighet og presisjon ble begrenset av både metodiske og systematiske forhold ved kartleggingen. Svak bildegeometri, med påfølgende svak kamerakalibrering, var sammen med plasseringen av kontrollpunkter kilder til betydelig romlig variasjon i terrengmodellenes presisjonsnivå.

Preface

This thesis concludes my Master of Science degree in Geology at Institute of Geoscience and Petroleum (IGP) at NTNU. The work has been conducted in collaboration with the Norwegian Public Roads Administration (NPRA), and over one year starting in september 2018. The fieldwork was conducted from January to March 2019.

Tore and Bjørn, thanks for your thoughtful advices, faith and patience. Special thanks to Tore for spending late nights correcting my is' and are's. Jan Helge, thanks for all the help during my field work, and for letting me play with expensive gear. Jens, thanks for letting me borrow your second home. Also thanks to Ole Andre and Tore M. for help during fieldwork, and to Stian and Paul for your interest and helpful mindset. And finally, Martine and Gunne, thanks for a year at the office with you, it's been a pleasure!

Contents

List of tables	ix
List of figures	xii
1 Introduction	1
2 Theory	3
2.1 Photogrammetric principles	3
2.2 SfM-MVS photogrammetry	4
2.3 SfM-MVS mapping of snow surfaces	6
3 Methods	9
3.1 Study area	9
3.1.1 Location	9
3.1.2 Geography and topography	10
3.1.3 Weather and climate	10
3.1.4 Avalanche character and frequency	11
3.2 Data acquisition	12
3.2.1 Survey areas	12
3.2.2 Survey procedures	13
3.2.3 dGNSS measurements	13
3.2.4 UAS image acquisition	13
3.2.5 Ground control points (GCPs)	16
3.2.6 Check points (CPs)	16
3.2.7 Weather data	16
3.3 Photogrammetric processing	16
3.3.1 Software	16
3.3.2 Workflow and settings	17
3.4 Model validation	20
3.4.1 Photogrammetric precision	20
3.4.2 Georeferencing accuracy	21
3.4.3 Georeferencing precision	21
3.4.4 Systematic errors	21
3.5 Surface change detection	21
3.5.1 Level of detection (LoD)	22
3.5.2 Snow depth calculation and validation	22
3.6 Measures of error, accuracy and precision	23

4	Results	25
4.1	Field surveys	25
4.1.1	Survey data	25
4.1.2	UAS and camera performance	28
4.1.3	dGNSS measurement precision	29
4.2	Photogrammetric processing	30
4.2.1	Image observations and initial network calibration	30
4.2.2	Camera model calibration	32
4.2.3	GCP analysis	35
4.3	DEM validation	37
4.3.1	Photogrammetric precision	38
4.3.2	Georeferencing accuracy	42
4.3.3	Georeferencing precision	42
4.3.4	Systematic errors	44
4.4	Snow depth maps	45
4.5	Snow depth change detection	47
4.5.1	Minimum level of detection	47
4.5.2	Weather data	47
4.5.3	DEMs of difference (DoDs)	50
5	Discussion	53
5.1	DEM precision and accuracy	53
5.1.1	Photogrammetric precision	53
5.1.2	Georeferencing precision	55
5.1.3	Systematic errors	56
5.1.4	Total georeferenced accuracy	57
5.2	Snow depth maps	58
5.3	Snow surface change detection	58
5.3.1	Methodical considerations	58
5.3.2	Detected periodical changes	58
6	Conclusions	61
	References	63
	Appendices	69
A	Survey and safety plans (turplaner)	69
B	GCP analysis	74
C	Photogrammetric precision	75
D	Georeferencing errors	77
E	Section profiles	77

List of Tables

3.1	Camera calibration models	19
4.1	Survey overview	25
4.2	UAV and camera settings	26
4.3	GNSS precision	29
4.4	Initial network calibration and filtering	30
4.5	Camera calibration steps	34
4.6	Accuracy and precision of final snow surface models	37
4.7	Snow depth errors on CPs	45
4.8	Change detection periods	47
4.9	Minimum levels of detection	47

List of Figures

2.1	Image geometry and bundle adjustment	4
2.2	Lens distortion patterns.	6
2.3	Photogrammetric uncertainties	7
3.1	Location of the study area	9
3.2	Monthly averages of temperature, precipitation and snow depth at Filefjell-Kyrkjestølane	10
3.3	Avalanche at Tyinstølen in 2008	11
3.4	Survey areas	12
3.5	Pictures from surveying	14
4.2	3D visualisation of Tyinstølen point cloud	26
4.1	Orthophotos of snow covered terrain and GCP/CP locations for the Tyinstølen surveys.	27
4.3	Flight path and camera positions	28
4.4	Image quality differences	30
4.5	Tie point observations	31
4.6	Tie point observations	32
4.7	Camera calibration effects on GCP and CP error	33
4.8	Camera calibration effects on surface geometry	33
4.9	GCP performance	35
4.10	Effect of GCP configuration on surface geometry	36
4.11	Image plane distortion plots	38
4.12	RMS reprojection errors on individual images	38
4.13	Spatial distributions of RMS reprojection error on individual tie points	39
4.14	Distributions of RMS reprojection error on individual tie points	39
4.15	Tie point precision distributions	40
4.16	Spatial distributions of vertical tie point precisions	41
4.17	Vertical errors on individual GCPs and CPs	42
4.18	Spatial distribution of errors on GCPs and CPs	43
4.19	Systematic error patterns in Lake Tyin DEM	44
4.20	Snow depth distributions	45
4.21	Snow depth maps	46
4.22	Weather at Langøddin, period P1-P3	48
4.23	Weather at Langøddin, period P4	49
4.24	Snow depth change distributions	50
4.25	Change detection in period P1 and P2	51
4.26	Change detection in period P3 and P4	52

1 Introduction

Snow avalanches are a natural hazard that puts humans and infrastructure at risk in mountainous regions all over the world. Naturally released avalanches pose the biggest threat to roads, buildings and other infrastructure, while avalanches triggered by recreational activities, such as skiing and snowmobile riding, have become a major cause of harm to humans (Schweizer et al., 2003). In Norway, more than 30 % of the roads and railroads are exposed to snow avalanche or rockslide hazard, and snow avalanches are the type of geohazard that causes the highest numbers of road closures (Frauenfelder et al., 2017). Due to the large number of avalanche sites and high cost of structural mitigation measures, non-structural measures based on short-term hazard assessment, such as early warning systems, have an important role in management of avalanche risk.

Avalanche hazard is determined by the probability of an avalanche to occur, and its potential to cause damage to something of value (Statham et al., 2018). On a regional basis, short-term hazard assessments are typically concerned with the likelihood of release, expected avalanche size and frequency, and the distribution of hazardous sites (Statham et al., 2018; EAWS, 2019b; Müller et al., 2016). The purpose of these, which often are presented as public bulletins, is to provide a basis for assessments at specific avalanche sites. Local hazard assessments, performed by recreationists as well as avalanche professionals, are necessary to determine actual risk. For the safety of infrastructure and transportation, the probability of spontaneous release and expected run-out length at a given time and place are key factors and decisive for whether active mitigation measures such as evacuation, closure or artificial release are initiated.

Avalanche formation is by Schweizer et al. (2003) described as "the complex interaction between terrain, snowpack, and meteorological conditions leading to avalanching". Although some important physical and mechanical aspects of avalanche formation are increasingly understood and modeled (Gaume et al., 2018), the complex interactions, and the resulting spatial and temporal variability of snow cover properties (Schweizer et al., 2008), make predictions of "where" and "when" inherently difficult. Operational hazard assessment and avalanche forecasting therefore mostly rely on assessment of empirically derived and physically meaningful *contributory factors* (Schweizer et al., 2003) to specified *avalanche problems* (EAWS, 2019a). A key factor for the formation of dry-snow slab avalanches, which forms the major type of avalanche hazard, is the loading of wind deposited snow on lee-slopes. Wind-drifted snow cause cohesive slabs to be formed, of which the volume and weight determines the stress on underlying weak layers as well as the potential run-out length of a possible avalanche. The likelihood of release is furthermore controlled by the time-scale and rate of loading (Birkeland et al., 2018).

Remote sensing methods are now used within a range of cryospheric disciplines, common applications including monitoring of snow and ice volumes (Tedesco, 2015) as well as detection and mapping of avalanches (Eckerstorfer et al., 2016). With regard to avalanche

formation, high-resolution mapping of snow depth distribution on the slope-scale has been performed to, among other things, explore the physical processes shaping the snow cover (Mott et al., 2010) and develop empirical prediction models (Schön et al., 2018). Terrestrial laser scanner (TLS) has proven useful for such measurements (Prokop, 2008; Deems et al., 2013), and in recent years, aerial photogrammetry has become a low-cost alternative thanks to the evolution of unmanned aerial systems (UASs) and modern image matching algorithms (Bühler et al., 2016). Although early efforts to measure snow depth with aerial photogrammetry were made long before the digital era (Smith et al., 1967; Norem, 1974), the obtainable accuracy has until recently been too low for most purposes.

A potential application of UASs now being investigated, is monitoring of snow cover properties as a tool in operational avalanche hazard assessment. This study was conducted in collaboration with the Norwegian Public Roads Administration (NPRA). It was aimed at investigating the applicability of readily available, consumer-grade UASs and aerial photogrammetry for quantification of snow loading in avalanche release areas, preferably during weather episodes associated with increasing avalanche danger. The research were governed by four main goals:

- Plan and conduct UAV aerial surveys of an avalanche release area before and after weather events leading to snow accumulation
- Produce digital elevation models (DEMs) using Structure-from-motion photogrammetry and describe and quantify the related uncertainties
- Compare DEMs and calculate changes in snow depth distribution
- Verify detected changes based on DEM precision and accuracy, and meteorological data from the events

This introduction intends to give the reader an understanding of the greater context in which the research was done. For more information on topics related to snow and avalanche formation, the reader is referred to the literature introduced here and to McClung and Schaerer (2006). In the next chapter, a brief theoretical introduction to photogrammetric principles and techniques is provided. Thereafter comes a description of the survey area and the methods used for data acquisition and processing, before the results are presented and followed by a discussion of the main findings. The last chapter contains the concluding remarks and suggestions for further research.

2 Theory

2.1 Photogrammetric principles

Photogrammetry is the science and technology of extracting information about physical objects from photographs (Förstner and Wrobel, 2016). Resolving geometric structures for mapping and surveying purposes, e.g. generation of topographic elevation models, is one of the main applications, and is today obtained with a range of different techniques. On one end is the traditional photogrammetric analysis, which is based on image pairs of line-preserving central perspective imagery, often taken normal to the surface and with known camera properties and poses (e.g. Kraus (1993)). On the other end, computer vision techniques now allow automated self-calibration of complicated networks from highly irregular image collections (e.g. Luhmann (2011); Förstner and Wrobel (2016)).

The fundamental parts of geometric reconstruction of a scene from images, independent of the specific technique used, are 1) camera geometry, 2) image geometry and 3) surface (scene) geometry (Förstner and Wrobel, 2016). The camera geometry is determined by the camera lens and sensor properties, and determines how the visible scene is projected onto the image plane (figure 2.1, left). The image geometry represents the camera poses (positions and orientations) in the same 3D space as the surface geometry, which is a sample of points, lines or surfaces representing the surface to be reconstructed. The reconstruction itself is based on the best-fit combined network of all three geometries, where the reconstructed surface is an extended set of surface features with their 3D positions determined from the camera and image geometry of the combined network.

The optimal combined network is obtained through what is called a 'bundle adjustment', in which the unknown parameters of the camera, image and surface geometries are simultaneously estimated across an arbitrarily large collection of images (Förstner and Wrobel, 2016). The 'bundle' represent the light rays connecting camera projection centres to the surface features that make up the surface geometry (figure 2.1, right), and the 'adjustment' refers to the minimisation of a non-linear cost-function reflecting the measurement error (Smith et al., 2015). The error term is usually based on the *re-projection error*, representing the distance between the true and the network-estimated location of surface features in the image plane (Förstner and Wrobel, 2016).

In traditional photogrammetric analysis, originally developed for analogous imagery and limited processing capabilities, camera geometry and either image or surface geometry has to be known for the bundle adjustment to be carried out (Westoby et al., 2012). The adjustment is then limited to finding the spatial relationship between camera positions and identified surface features. This require the use of so-called metric cameras, maintaining a constant and well defined geometry throughout the image acquisition, and precisely measured 3D coordinates of either camera positions or a series of control points distributed across the surface to be reconstructed.

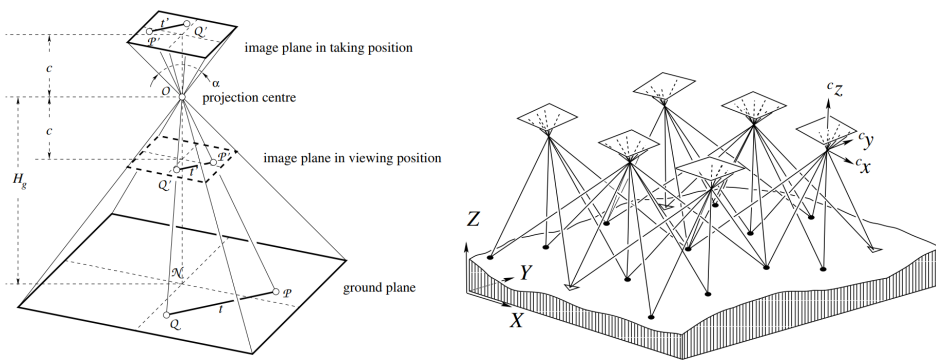


Figure 2.1: Left: Undistorted projection of flat ground onto the image plane in an aerial image, where camera geometry is represented by the principal distance c and the viewing angle α . (From Förstner and Wrobel (2016), figure 12.1, p. 457) Right: The 'bundle' within the bundle adjustment, in which image observations of surface features is used to estimate camera, image and surface geometry. (From Förstner and Wrobel (2016), figure 11.12, p. 450)

2.2 SfM-MVS photogrammetry

In contrast, more recently developed methods allow bundle adjustments without any prior knowledge of the involved geometries (Westoby et al., 2012). 'Structure-from-Motion' (SfM) represents together with 'Multi-View Stereo' (MVS) a new generation of photogrammetric reconstruction techniques that combine classic photogrammetric principles with computer vision image matching algorithms (Smith et al., 2015). Put together, they provide a complete and automated workflow for creating dense 3D point clouds from a set of overlapping images, where unscaled surface geometry can be reconstructed from image information only. The SfM part, as the name suggests, estimate network geometries based on images from a 'moving' camera, providing multiple offset views to all parts of the scene of interest (Westoby et al., 2012; Fonstad et al., 2013). A MVS algorithm is then commonly used to reconstruct the surface geometry from estimated camera and image geometries through a dense feature detection and matching process (Smith et al., 2015).

SfM-MVS combined with high resolution digital imagery acquired using UASs is a survey method that has been proved useful in a range of geomorphological and topographical studies (see e.g. Smith and Vericat (2015); Carbonneau and Dietrich (2017)). The method is capable of producing point clouds comparable to those obtained by terrestrial laser scanning (TLS) both in point density and accuracy, although SfM-MVS survey precisions are more dependent on factors specific to each individual survey (Smith et al., 2015).

General workflow

An overview of the general SfM-MVS workflow is provided in Smith et al. (2015), including references to where details on the mathematical operations can be found. Although the specific workflows implemented in different software will vary, they usually share a set of common characteristics. Starting with a collection of images covering a scene from

multiple viewpoints, the common SfM-MVS processing steps can be outlined as follows:

1. **Feature detection.** Identification of unique pixel sets, often called 'keypoints', in each image. The pixel sets are normalized for invariance to changes in orientation, rotation, scale and illumination.
2. **Keypoint matching.** Identification of corresponding keypoints, checking for correspondance above a certain threshold across a large number of keypoint descriptors.
3. **Identification of geometrically consistent matches.** Filtering of corresponding keypoints by considering the likely geometrical relationship between images with corresponding keypoints.
4. **Structure from motion.** Bundle adjustment with simultaneous estimation of keypoint coordinates (surface geometry), image geometry and camera geometry, using identified keypoint matches and the camera parameters available in EXIF tags as a starting point. The output is an unscaled sparse point cloud, along with estimated camera properties and poses.
5. **Scale and georeferencing.** Scaling of surface and image geometry by 1) identification of georeferenced ground control points (GCPs) or 2) assigning known camera pose information from GPS and IMU measurements.
6. **Refinement of parameter values.** Repeated bundle adjustments considering both image observation and georeferencing errors.
7. **MVS dense image matching.** Generation of a dense point cloud based on the established surface, image and camera geometries.

Camera calibration

A key element in the SfM bundle adjustment is the 'self-calibration' of camera geometry, where a camera model describing camera lens and sensor properties are estimated. While sensor properties, such as size and resolution, are fixed and given by the camera used, most lenses are associated with significant optical distortion that needs to be characterised and corrected. Lens distortion cause incorrect angles and curved lines in the projected image, and is a result of both lens design and quality. Consumer-grade lenses with a wide field-of-view is generally associated with large distortion, often of the complex type illustrated in figure 2.2. This type is especially difficult to compensate for by standard camera model parameters. Additionally, low-quality lenses often suffer from more random distortion patterns due to fabrication error. For further details on practical camera and camera calibration considerations, the papers by Mosbrucker et al. (2017) and Carbonneau and Dietrich (2017) are recommended.

Uncertainties and error sources

Final precision and accuracy of produced surface models depends on a range of factors related to the aerial survey as well as the photogrammetric processing. Detailed explanation of these factors and their influence is provided by James and Robson (2014)

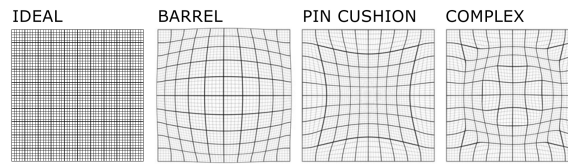


Figure 2.2: Illustration of common lens distortion patterns. The complex type is often found for small-format digital cameras with wide-angle lenses. (From Carbonneau and Dietrich (2017))

and James, Robson, d’Oleire Oltmanns and Niethammer (2017), while an overview based on these papers is given here. Errors are commonly divided into three main types: photogrammetric, georeferencing and systematic. The photogrammetric precision represent the uncertainties within the internal, photogrammetric network (figure 2.3), and is mainly determined by the number and quality of image observations, camera calibration quality and the strength of the image geometry, i.e. high overlap and converging viewing angles.

Georeferencing errors represent the difference between the reconstructed and the actual surface geometry after introduction of ground control points or recorded camera positions. These can be assessed in terms of the accuracy and precision, where accuracy represent measured differences and precision the uncertainty in surface shape, scale, translation and orientation resulting from the georeferencing process. Georeferenced accuracy and precision is mainly influenced by GCP distribution and positioning accuracy, and the weighting of this accuracy within the bundle adjustment. Obtainable accuracy is also expected to linearly degrade with range, with a theoretical ratio between RMSE (root-mean-squared error) on control points and viewing distance of about 1/1000 (James and Robson, 2012).

Systematic errors are the errors in surface geometry or image observations caused by erroneous camera geometry, typically resulting from uncorrected lens distortion, rolling shutter distortion or motion blur. They are often difficult to identify from errors on control points, but may cause considerable deformation to final DEMs. One common type of deformation is dishing/doming caused by radial lens distortion, often resulting from parallel viewing directions hindering proper camera calibration.

2.3 SfM-MVS mapping of snow surfaces

The potential of high-resolution mapping of snow surfaces using MVS-SfM photogrammetry has in recent years been explored within a range of different research fields. A number of studies has been aimed at the need for large-scale mapping of snow depth distribution for hydrological, ecological and climatological purposes (Bühler et al., 2015; Nolan et al., 2015; Harder et al., 2016; Cimoli et al., 2017; Eberhard et al., 2018). Snow depth mapping at smaller scales and higher resolutions has been investigated both in general terms (Vander Jagt et al., 2015; Bühler et al., 2016; De Michele et al., 2016; Avanzi et al., 2017; Bühler et al., 2017; Fernandes et al., 2018) and with the purpose of monitoring snow ablation (Eker et al., 2019), change detection in avalanche release areas (Prokop et al., 2015; Peitzsch et al., 2018), avalanche examination (Gauthier et al., 2014; Ecker-

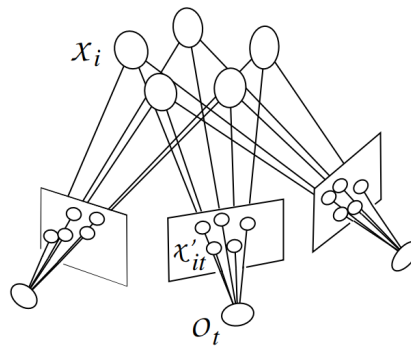


Figure 2.3: Relation between uncertain image observations, image geometry and surface geometry. (From Förstner and Wrobel (2016), figure 1.8, p. 10)

storfer et al., 2015; Conlan and Gauthier, 2016; Peitzsch et al., 2016), avalanche powder cloud monitoring (Dreier et al., 2016) and evaluation of snow fences (Basnet et al., 2016).

The most used setup for slope-scale surveys of snow depth is a multirotor UAS with a small format digital camera, and georeferencing through ground control points (GCPs) measured with dGNSS. Potential and limitations of such a method is summarised in Bühler et al. (2016). One of the major challenges is the amount of surface features available for the image matching algorithm, and smooth snow surfaces and flat light can result in poor image observation quality and noise in the surface model. Bühler et al. (2017) therefore investigated the use of near-infrared imagery, obtaining promising results. Reported errors on UAS snow depth measurements, as compared to manual probing, for five studies range from 7 to 45 cm (RMSE). Georeferenced errors in the surface models are found between 3.6 and 23 cm for independent check points, and between 1.2 and 4.8 cm for control points used for georeferencing and included in the bundle adjustment.

3 Methods

3.1 Study area

3.1.1 Location

The survey areas were located in the Tyin area in the southwestern corner of the Jotunheimen mountains in Southern Norway. The county road between Tyin and Årdal (Fv. 53) is in this area exposed to several avalanche paths, mainly along the southern part of Lake Tyin and in the valley towards Tyinkrysset. Avalanches used to pose a significant threat to road users and snow clearing operations, and the road were frequently closed due to avalanche danger.

Since 2016, the Norwegian Public Roads Administration (NPRA) has protected the road by a preventive avalanche release system from Wyssen Avalanche Control AG. The system comprises 14 avalanche towers placed in the most critical avalanche release areas (see figure 3.1), containing charges of explosives that can be remotely detonated, and a local avalanche warning system based on manual observations and weather prognoses. Avalanches can then be released in a controlled way before they get large enough to hit the road, or if the risk of naturally triggered avalanches already is high.

The avalanche danger in the Tyin area is proven to be strongly connected to drifting

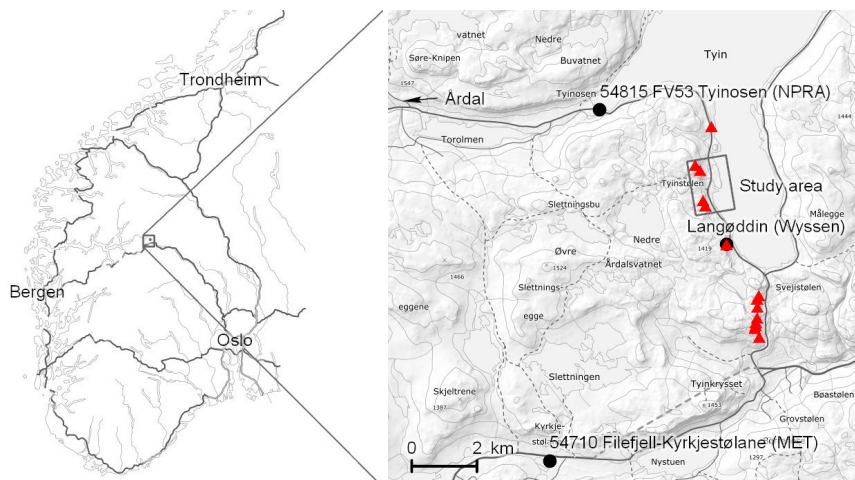


Figure 3.1: Location of the study area at Tyin in Southern Norway. Red symbols show the location of Wyssen avalanche towers along the road, and black symbols show nearby weather stations. (©Kartverket)

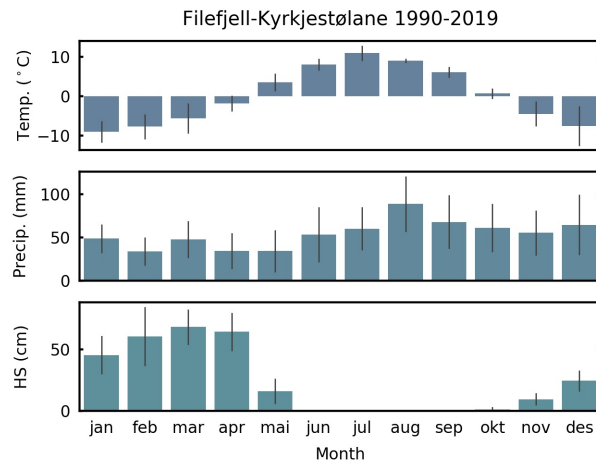


Figure 3.2: Monthly averages of temperature, precipitation and snow depth (HS) at the Filefjell-Kyrkjestølane weather station in the period 1990-2019. Error bars represent one standard deviation. (Source: eklima.no)

snow events, which are usually frequent throughout the winter season. As such, there is an operational need to understand and evaluate the loading in release areas during such events. For research purposes, the artificial triggering of avalanches provide possibilities of relating measurements and predictions to actual avalanches, and many of the release areas are safely and easily accessible for various types of measurements.

3.1.2 Geography and topography

Jotunheimen is part of the larger mountain range called the Scandinavian Mountains, which runs north-south and divides the steep valleys and fjords of Western Norway from the more gentle hills and lowlands of Eastern Norway and Sweden. Lake Tyin is draining westward from the outlet at Tyinosen, but is located more or less at the watershed between Eastern and Western Norway. The lake is at 1084 m a.s.l. situated just above the tree line, and the southern part is surrounded by hills reaching up to about 1440 m a.s.l. In general, these hills are characterised by gentle to moderately steep slopes abrupted by some steeper sections and cliffbands.

3.1.3 Weather and climate

Monthly averages of temperature, precipitation and snow depth from the weather station at Kyrkjestølane (location in figure 3.1) are shown in figure 3.2. The snow season usually starts in late October or early November and ends in May, with peak snow depths often found in March-April. However, the large variations in average temperature and precipitation, especially during the first part of the winter, indicate that the snow cover may develop significantly different from year to year. Winter weather is typically controlled by either

low-pressure systems off the western coast of Norway, often giving mild temperatures, large snowfalls and strong winds from SW to NW, or high-pressure systems in east, which give colder temperatures, less precipitation and calmer winds.

3.1.4 Avalanche character and frequency

About hundred avalanches were recorded during each of the first two seasons artificial avalanche release was performed (Wyssen Norge AS, 2018, pers. comm.). Especially along Lake Tyin, several avalanches were crossing the road each season. A large part of the avalanches was dry-snow slab avalanches, largely formed by wind-deposition of snow during episodes of strong winds from a westerly direction. Avalanches in the area are historically associated with abnormally long run-out lengths, well illustrated by the major avalanche in 2008 (figure 3.3).



Figure 3.3: A large avalanche crossed the road and also hit buildings at Tyinstølen in January 2008. The runout length were over 600 m, despite a height difference of only around 170 m (Håland et al., 2015). The survey area called *Tyinstølen* in this study cover the left part of the release area seen on the picture. (Svein Helge Frækaland/NPRA)

3.2 Data acquisition

3.2.1 Survey areas

Photogrammetric survey plans were prepared for three main avalanche release areas close to Tyinstølen on the western side of Lake Tyin, hereby called *Tyinstølen*, *Støl* and *Mel* (see figure 3.4). *Støl* and *Mel* cover two major release areas where avalanche towers are installed. *Tyinstølen* cover the southern part of the release area of a major avalanche in 2008 (figure 3.3), where both natural and skier-triggered avalanches are regularly released. *Tyinstølen* was given the highest priority in this work due to easy access, favourable placement of ground control points and because any snow cover changes most likely would remain undisturbed by avalanche control operations. If snow cover changes at *Tyinstølen* could be successfully captured, the next step would be to perform surveys of the areas *Støl* and *Mel* to investigate the relation between snow deposition and produced avalanches.

A survey area in non-avalanche terrain, named *Lake Tyin*, was also defined to investigate sources and magnitudes of error related to the survey setup and the photogrammetric processing. For easy validation of surface geometry and detection of any systematic deformation, e.g. doming/dishing, this area was placed on a completely flat snow surface at Lake Tyin. Area size and shape were set to resemble the size and shape of *Tyinstølen* to make the error evaluation as relevant as possible.

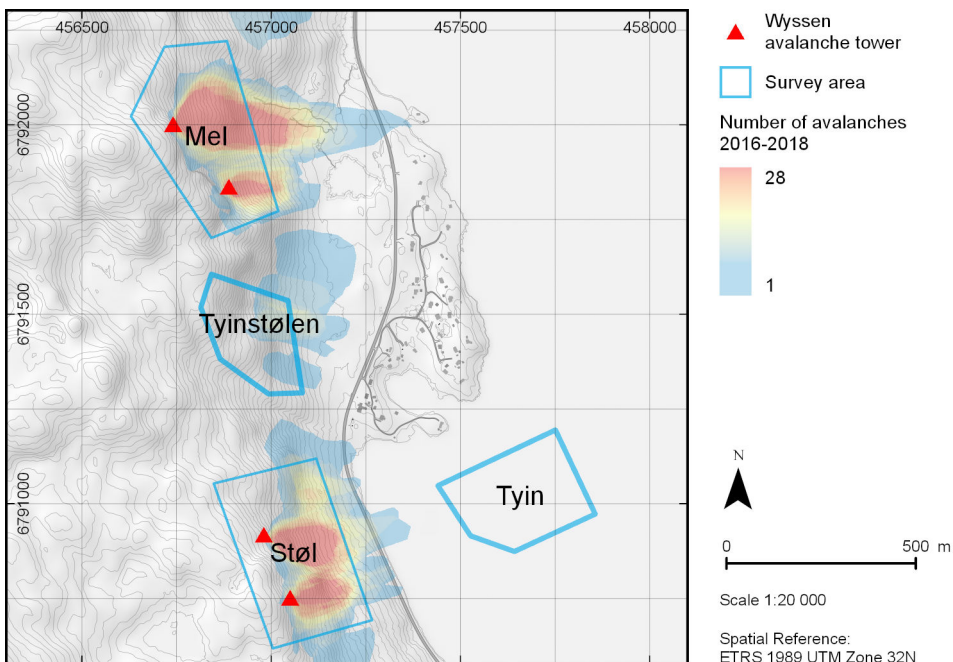


Figure 3.4: Overview of the survey areas, of which *Tyinstølen* and *Lake Tyin* were prioritised in this work. The avalanche 'heat map' shows the extent of all avalanches, both naturally and artificially released, registered during the seasons 2016-2017 and 2017-2018. (Data: Wyssen Norge AS/Map: ©Kartverket)

3.2.2 Survey procedures

Surveys were conducted by first performing dGNSS and snow depth measurements at each pre-defined *ground control point* (GCP) and *check point* (CP). The UAS survey was then carried out from a pre-defined take-off point, before doing a second round of dGNSS measurements of the GCPs. Using alpine touring skis for transportation, surveys could be completed by one person alone in less than two hours. Survey plans can be found in appendix A.

3.2.3 dGNSS measurements

Precise positioning was obtained with a Trimble Geo7X RTK hand-held dGNSS receiver mounted on a telescopic pole. The receiver was using a mobile connection to access real-time correction data from the CPOS service from the Norwegian Mapping Authority. CPOS is short for "centimetre positioning", and the stated achievable measurement accuracy is 8 mm horizontally and 17 mm vertically, given by one standard deviation, in areas where the distance between permanent GNSS reference stations is around 35 km (Statens kartverk, 2019). The system calculates a virtual base station based on data from reference stations and the position of the receiver, which treats the correction data as if they were from a physical local base station. Recommended time between repeated measurements of the same point is minimum 45 minutes for a total of two measurements, and minimum 20 minutes for a total of three measurements.

The reference stations closest to the survey areas are located at Tyinkrysset (6 km southward), Årdalstangen (25 km westward) and Hegge (45 km eastward), and correction data were expected to be reasonably precise. The number of available satellites was observed to be between 10 and 16 during most measurements.

3.2.4 UAS image acquisition

Setup

Aerial imagery were obtained with a simple setup comprising a DJI Mavic 2 Zoom UAS and an Ipad with the flight control app Litchi installed. The Mavic 2 Zoom is a small and lightweight consumer-grade UAS that can operate in temperatures down to -10 °C and wind speed up to 10 m/s (DJI, 2019). The built-in camera has 24-48 mm (35 mm equivalent) lens and a 1/2.3" CMOS sensor with a pixel resolution of 4000 x 3000. Expected flight time is according to the manufacturer 31 minutes in optimal conditions, and 25 minutes for an average flight. Cold temperatures and windy conditions were expected to reduce battery life significantly and had to be accounted for in survey design.

To efficiently capture photos with the desired overlap and ground resolution, all flights were performed autonomously according to predefined flight plans. The Mavic 2 Zoom uses a GPS/GLONASS unit and a barometer for navigation. The stated hovering accuracy is ± 1.5 m horizontally and ± 0.5 m vertically, which is accurate enough for following a survey grid. A slight vertical drift during flight has been reported by other Mavic users, supposedly because the barometer altitude may change with sensor warming.

Autonomous flying is not supported by the original DJI Go flight control app, but is possible through a number of third-party apps. Among these is Litchi, which is a low-cost



Figure 3.5: Pictures from surveying. Upper left: Tyinstølen survey area seen from the parking lot (Fv. 53 in the foreground). Upper right: Survey backpack with all the required equipment. Lower left: Snow probe, dGNSS receiver and GCP target plate. Lower right: DJI Mavic 2 Zoom. (All photos: Emil Solbakken)

alternative based on a flight control app and an online account where flight plans can be stored and accessed. Flight plans can be exported and imported as csv-files, allowing for use of specialised flight planning software.

Flight planning

Aerial surveys for conventional photogrammetry are typically based on capturing photos orthogonal to an assumed horizontal ground (*nadir*) at regular intervals along parallel flight lines (*strips*) (Kraus, 2007; Pepe et al., 2018). Flight height, photo interval and the distance between flight lines are then determined by the camera's field of view and sensor resolution, and the desired sampling resolution, overlap and sidelap of the survey. These principles, combined with autonomous flying, allow fast and simple image acquisition, and has been shown applicable also for SfM photogrammetry (Clapuyt et al., 2016; De Michele et al., 2016; Avanzi et al., 2017).

However, several studies have emphasized the importance of image geometry on the quality of SfM-based reconstructions (James and Robson, 2014; Carbonneau and Dietrich, 2017). SfM algorithms are designed to work with convergent imagery at varying scales, and covering the points of a scene from a wider range of viewing angles than what is

obtained with parallel images makes the self-calibration more precise and reduces the need for GCPs to prevent systematic errors (James and Robson, 2014; Mosbrucker et al., 2017). General recommendations for practical flight plans can be found in the aforementioned literature and in Smith and Vericat (2015). In summary, a recommended approach is to combine parallel imagery from a conventional grid with high overlap (> 80 %), providing efficient and reliable coverage at the desired ground resolution, with oblique imagery (< 20° angular change, > 40° angle of incidence) at a larger scale, providing convergent views of the scene.

The flight plans used in this study were designed based on conventional principles only, which had some major disadvantages that became apparent during the SfM processing. Flights were planned as a compromise between maximising ground resolution, overlap and area coverage on one side, and operational regulations, limited battery life and the risk of motion blur and rolling shutter effects on the other. Grids with two different GSDs were made: one with flying height 80 m and GSD 2.8 cm/pixel, and one with flying height 70 m and GSD 2.5 cm/pixel. These represent average values obtained with a planar flight grid tilted parallel to the best-fit plane of the survey area, the flying height representing the perpendicular distance between the planes. For both flying heights, the camera were tilted perpendicular to the average ground plane. Photo intervals were set to 2 s (the minimum value), providing 86 % overlap at flying speeds of 7 m/s (height 70 m) and 8 m/s (height 80 m). With sidelaps, determined by the distance between flight strips, of around 77 %, total flight times were estimated to 10-12 minutes.

The flight grids were made by first fitting a plane to the DTM within the survey area using CloudCompare¹, producing an 'average' hillslope represented by its dip angle and dip direction. A horizontal grid with strips in the across-slope direction were then created in MissionPlanner², before transforming grid coordinates and calculating UAS and camera settings in an Excel worksheet. Grid transformation consisted of vertical and along-slope shifting of grid coordinates to obtain a grid parallel to the fitted plane and with the desired slope-normal distance and field of view. Grid elevations were then set relative to the planned take-off point, to avoid flying heights being affected by inaccurate vertical GPS-positioning. The UAS heading were set to always be normal to the mean slope orientation, with the camera tilted perpendicular to the average slope angle.

Camera parameters

Images were captured at minimum focal length (maximum field of view) and with fixed aperture and automatic adjustment of shutter speed and ISO-value. Maximum frame rate at full resolution were 0.5 frames per second in JPEG format and 0.2 frames per second in RAW format. The low frame rate required images to be saved in JPEG format, and adjustment of the flying speed to obtain the planned overlap. Focus was set at the beginning of each survey and not changed afterwards.

¹www.danielgm.net/cc/

²www.ardupilot.org/planner/

3.2.5 Ground control points (GCPs)

Ground control points to be used for surface model georeferencing were established at pre-defined locations and marked by either spray painted crosses or home-made target plates (see figure 3.5). The target plates could stay deployed for long time periods and remained visible also when snowdrift occurred during surveying, and were used in all surveys of the Tyinstølen area. All target centre positions were measured twice, with the setup and procedure described in section 3.2.2-3.2.3.

To be able to conduct surveys of avalanche release areas also during periods of high avalanche danger, the GCPs were placed in safely accessible areas above or around the area of interest. Ideally, GCPs should be evenly distributed and cover the full survey area, and the consequences of a limited GCP network is both reduced accuracy and reduced control of the accuracy in the parts of the survey area that are not covered. Recommended GCP density depend on the required survey accuracy, although James, Robson, d’Oleire Oltmanns and Niethammer (2017) emphasize the importance of image geometry and distribution of GCPs rather than the exact density for SfM surveying.

For precise scaling and orientation, it is strongly recommended to have GCPs at least in all corners of the survey area. This was not obtained around any of the release areas, and without control measurements in large parts of the surveyed area, an important part of the DEM validation was to estimate the uncertainty related to limited GCP distribution.

3.2.6 Check points (CPs)

Check points represent in this study unmarked reference points used for validation of vertical surface model accuracy. Single dGNSS-measurements and vertical snow depth measurements with a probe were performed at each point. The CPs were placed close to (1-2 m away from) and roughly halfway between the GCPs.

3.2.7 Weather data

Weather observations with 10 mins resolution from the weather station at the Langøddin avalanche tower (see figure 3.1) were obtained from Wyssen Norge AS. Observations included precipitation, temperature, wind speed and wind direction.

3.3 Photogrammetric processing

3.3.1 Software

Photogrammetric reconstruction were performed using Agisoft Metashape Professional (version 1.5), formerly called PhotoScan. This is a widely used SfM-MVS software providing a complete workflow from the import of raw imagery to the export of dense point clouds, tiled models, DEMs and orthophotos. Software functions can be accessed either through a graphical interface or by Python scripting, the latter providing extended access to processing data and the possibility of autonomous processing. The software were run on a medium-sized workstation laptop (quad-core Intel Core i7 2.8 GHz CPU, 32 GB RAM, Nvidia Quadro K2100M GPU with CUDA-support).

According to memory requirements stated by Agisoft, the installed RAM should accommodate processing of sets of up to 500 photos with the highest quality settings. The processing time in such a case, however, would be extremely long due to the limited capacity of the CPU and GPU. The image sets in this work consisted of 250-350 photos with 75-85 % overlap, and the generation of sparse and dense point clouds took 0.5-1 and 4-6 hours, respectively, producing final dense clouds of medium quality with point resolutions of around 0.1 m .

3.3.2 Workflow and settings

Processing workflow and settings were initially based on recommendations provided in the Metashape user manual (Agisoft, 2018a). The user manual explains, however, just briefly what goes on inside the algorithms, and other sources and some trial and error were needed to appropriately evaluate the influence of input parameters and to ensure the quality of the output. The following general workflow is largely based on the work by James, Robson, d'Oleire Oltmanns and Niethammer (2017); James, Robson and Smith (2017), representing a new standard for analysis and reporting of uncertainties in topographic surveys processed with SfM-MVS. The Agisoft user forum³, where tips and tricks are shared by both Metashape users and developers, was a valuable resource for software-specific information. So was the Metashape Python reference (Agisoft, 2018b), providing the necessary information to access data and functions through Python scripting.

Photo import

Photos were imported as original jpeg-files with a resolution of 4000 x 3000 pixels. Image metadata included camera settings and recorded photo positions and poses. Metashape offers automatic estimation of the quality of input images, e.g. to sort out poorly focused images. Quality values are given based on the highest observed sharpness level in each image, and images with estimated quality below 0.5 are recommended excluded from processing (Agisoft, 2018a). Obtained image qualities were generally well above this threshold, but for surveys in sub-optimal light conditions lower-quality images had to be accepted for the whole scene to be covered.

Image observations and initial network calibration

The initial network was created with the 'Align photos' function, which based on imported photos performs three main operations and results in a 'sparse point cloud':

1. Key point identification: Automatic detection of image features that can be matched across photos.
2. Point matching: Key points being identified in two or more photos are matched and become tie points binding images together.
3. Self-calibrating bundle adjustment: Initial estimation of the best-fit network of 3-D tie point coordinates (making up the sparse cloud) and camera parameters and poses.

³www.agisoft.com/forum

Alignment settings include alignment accuracy, the maximum numbers of key points and tie points allowed in each photo, how matching points are searched for and parameters to include in the camera calibration model. Following James, Robson and Smith (2017), all surveys were processed with accuracy 'high' (images are processed at their original resolution), key point limit '40,000' (default value), tie point limit '5,000' (default value is 4,000) and preselection 'generic' (overlapping photos, 'pairs', determined at lower resolution prior to point matching).

The initial camera self-calibration were set to comprise the parameters principal distance (focal length) F , principal point offset C_x, C_y and radial distortion terms K_1, K_2, K_3 as recommended by James, Robson, d'Oleire Oltmanns and Niethammer (2017). Three distortion terms might be superfluous for standard consumer cameras, and the influence of each term were therefore evaluated later in the process to prevent over-parameterisation.

After alignment, the sparse point cloud were checked for obvious outliers, poor matches and high or systematic image residuals. This process involved visual inspection of the sparse cloud, point filtering with the 'Gradual selection' tool and evaluation of image residuals across individual images and in total for all tie points. Tie points were removed if 1) clearly located off the surface, 2) observed in only two images, and 3) through gradual selection of the points with the lowest scores on the quality metrics 'Reprojection error' (large image residuals), 'Reconstruction uncertainty' (low precision due to small baseline) and 'Projection accuracy' (inaccuracy related to tie point size) (Agisoft, 2018a). Tie points were removed gradually and along with repeated bundle adjustments, which in Metashape is carried out using the function called 'Optimize cameras'.

Tie point filtering and bundle adjustments were continued until the RMS of image residuals were below 1.5 pixels and no single images or tie points showed noticeably higher image residuals. Tie point precision were further investigated by enabling estimation of tie point covariances during bundle adjustments. The model view called 'Point Cloud Variance' shows the uncertainty of estimated tie point coordinates, visualised by the longest axis of the error ellipsoid of each tie point.

Reference markers were established by identifying GCPs in images using the 'guided approach' described in the user manual (Agisoft, 2018a). This process involves 1) import of GCP coordinates from the related dGNSS survey, 2) manual location of markers in two images each, 3) automatic projection of approximate marker locations to the rest of the images, and 4) manual refinement of each marker location. The centre of the deployed GCP targets were generally easy to locate within sub-pixel accuracy, and were otherwise discarded.

Markers were first included in a bundle adjustment as image observations only, to assess their associated image residuals. Fitting the 'inner constraints' sparse cloud (self-calibrated without 3D reference points (James, Robson, d'Oleire Oltmanns and Niethammer, 2017)) to marker ground coordinates, by scaling and orienting only, indicated how well the 3D geometry were reconstructed from image information only. Ground coordinates were then included in the network for further bundle adjustments, requiring three accuracy metrics to be set for correct weighting of errors in the bundle adjustment. 'Marker accuracy (m)' (precision of ground coordinates) were set as the RMSE of dGNSS measurements, 'Marker accuracy (pix)' (precision of marker observations) were set as the RMS image residuals of the markers, and 'Tie point accuracy (pix)' (precision of tie point

observations) were set as the RMS image residuals of tie points. These settings follow suggestions in James, Robson, d'Oleire Oltmanns and Niethammer (2017), and were used as a general starting point for the final processing.

Camera model calibration

Following the suggestions in James, Robson and Smith (2017), it was verified that parameters included in the final camera model 1) improved the results, 2) had magnitudes that exceeded the precision to which they were determined, and 3) were not strongly correlated. Improvements/decrements to the surface model were assessed by changes in RMS reprojection errors and marker errors, and the precision and correlation of camera parameters were evaluated using the correlation table and distortion plots available in Metashape.

The most critical terms in the Brown-Conrady calibration model are F , C_x , C_y , K_1 and K_2 (Carbonneau and Dietrich, 2017). K_3 , which was included in the initial camera model, and tangential distortion terms P_1 and P_2 can also be significant, but require a stronger network geometry to be accurately resolved. The appropriate parameter set for the specific camera that were used was determined by considering one of the surveys at Tyinstølen (19.03.2019), which included a strip of oblique imagery and hence were assumed to have the strongest network geometry. With the initial camera model (model B) as a starting point, the effects of excluding K_3 (model A) and including P_1 and P_2 (model C) were assessed.

Table 3.1: Camera calibration models.

Model	Parameters
A	f, C_x, C_y, K_1, K_2
B	$f, C_x, C_y, K_1, K_2, K_3$
C	$f, C_x, C_y, K_1, K_2, K_3, P_1, P_2$

Metashape offers a 'rolling shutter compensation' to be included in the camera calibration, apparently comprising both rotational and translational transformation components (Agisoft, 2018b). The camera that were used utilises a rolling shutter, and signs of blur caused by this were apparent in some images. Each camera model were therefore calibrated with and without the rolling shutter compensation and the results compared.

As the self-calibration is largely dependent on the relative weighting of control points and tie points, the effects of varying ground control accuracy were also investigated. Bundle adjustments were run for a range of different ground control accuracy values for each camera model, similar to the approach used by James, Robson, d'Oleire Oltmanns and Niethammer (2017). Due to the relatively low number of deployed GCPs, all markers were included in the bundle adjustments. The CPs were then used to assess the vertical error on independent points by creating meshed DEMs of 1 m resolution from each sparse cloud and computing the point-to-mesh distance in CloudCompare.

Over-parameterisation, insufficient network geometry or overfitting to ground control points can cause self-calibrated camera models to produce systematic 'doming' errors in resulting DEMs (James and Robson, 2014; Carbonneau and Dietrich, 2017). The presence of such effects is normally hard to reveal from control point errors only, and it was assumed

impossible in this project due to the limited distribution of GCPs. The self-calibrated camera models were therefore used to process a survey of the flat snow surface at Lake Tyin. Systematic deformation could then be identified by looking for large-scale non-planarity in the resulting DEMs.

GCP analysis

With the appropriate camera model and accuracy settings established, the influence of GCP configuration on scaling, translation and orientation were investigated using a simplified version of the GCP analysis described in James, Robson, d'Oleire Oltmanns and Niethammer (2017). The analysis were aimed at evaluating the performance of individual GCPs, and estimating the sensitivity of the final surface shape and orientation to the distribution of GCPs.

Bundle adjustments were carried out for all possible combinations of 6-8 enabled GCPs, resulting in a total of 37 sparse clouds. The standard deviation of each tie point in vertical and horizontal direction, respectively, were then computed to investigate the spatial distribution of probable error magnitudes. The RMS of the standard deviations of each sparse cloud were then inspected for major outliers. It was also verified that the sparse cloud with all GCPs enabled had a low RMS value, hence being spatially close to the mean sparse cloud and representing a probable approximation of the true scene geometry.

Dense point cloud generation and surface model export

Dense point clouds were generated with quality 'medium' and depth filtering 'aggressive'. The quality setting determined the resolution at which the dense matching was performed ('medium' represents one fourth of the image resolution) (Agisoft, 2018a). Higher resolution would have required significantly longer processing time, and were not regarded as beneficial given the smooth snow surface and the achievable survey precision. The depth filtering option sets the allowed depth difference between neighbouring points, and determine both the potential level of detail and level of noise in the final point cloud. 'Aggressive' represents the highest level of filtering. This setting were found to reduce noise to a minimum, which were regarded as more important than preserving small-scale surface structures. Final models were exported as dense point clouds and DEMs with 0.1 and 0.25 m resolution, along with orthophotos with 0.025 and 0.1 m resolution.

3.4 Model validation

Accuracy and precision of the final models were evaluated in terms of photogrammetric precision, representing the precision of the internal, photogrammetric network geometry, and georeferencing accuracy and precision. Georeferencing accuracy is measured by errors on GCPs and CP, and precision represents the uncertainty of overall surface shape and orientation.

3.4.1 Photogrammetric precision

Reprojection errors on individual images is the standard measure given by the Metashape software and was exported directly, while tie point reprojection errors, covariances and

number of observations were accessed through the Python interface in Metashape. The covariance matrix represents the 3D variance of estimated tie point locations, and precision magnitudes and their spatial distribution were investigated by calculating the standard deviation in horizontal and vertical direction on each tie point. Reprojection errors were used as a measure of the image observation quality and general strength of the photogrammetric network, and tie point precisions as the resulting uncertainty in surface geometry.

3.4.2 Georeferencing accuracy

The final three-dimensional error on GCPs were exported from Metashape. Error on CPs were determined by computing the vertical distance from CP coordinates to the model surface. For dense point clouds, distances were computed with the M3C2 plugin in CloudCompare with projection scale d set to 0.4 m (see section 3.5 and Lague et al. (2013) for explanation). For the DEMs, distances were computed as the elevation difference between CPs and their nearest raster cell with no interpolation applied.

3.4.3 Georeferencing precision

The precision of the final surface shape and orientation is related to many different aspects of the photogrammetric processing, and is not easily quantifiable. Two of the main aspects is the relative weighting of GCPs and tie points during bundle adjustment, and the final scaling, translation and orientation by fitting the network of GCPs in the internal surface geometry to the network of GCP ground coordinates. Uncertainties related to these aspects were estimated based on the ratios between GCP and CP error, and the GCP analysis described in section 3.3.2.

3.4.4 Systematic errors

Surface model shape is often also subject to non-random error or uncertainty arising from methodical or technical restraints. In SfM photogrammetry, and especially using consumer-grade cameras, such errors are typically caused by insufficient or erroneous camera calibration (James and Robson, 2014). Related to this is also the effects of motion blur and rolling shutter distortion. Systematic errors are not necessarily reflected in neither errors on GCPs or CPs nor any other directly available measure of precision and accuracy. The presence and effects of such errors were therefore evaluated based on visible structures in the final DEMs, general observations during processing and the investigation of dishing/oming in the Lake Tyin DEM, as described in section 3.3.2.0.3.

3.5 Surface change detection

According to Lague et al. (2013), three main methods are used to estimate surface change from elevation models in geomorphological studies: DEM of difference, cloud-to-cloud comparison and cloud-to-mesh comparison. DEM of difference, or DEM subtraction, is the most used for measurements of vertical change and involve pixel-by-pixel subtraction of equally gridded DEMs. Cloud-to-cloud and cloud-to-mesh methods is based on calculating three-dimensional distances from point to point or from points to a surface mesh,

and are suitable for measurements in steep or complex terrain. A much used cloud-to-cloud method, originally developed for analysis of TLS data, is the 'Multiscale Model to Model Cloud Comparison' (M3C2) introduced by Lague et al. (2013). This method is based on calculating surface normals and the average distance between two clouds at a specified scale, incorporating confidence intervals to deal with uncertainty caused by local surface roughness. ? has investigated the applicability of M3C2 for snow depth calculations in SfM-MVS based studies, but the majority of such studies has been based on DEMs of difference with varying resolutions.

With the purpose of estimating snow deposition in avalanche release areas, DEM subtraction providing vertical change at 0.1 m resolution were considered to be a simple and precise method. Surface normal calculations with the M3C2 method could have provided precise three-dimensional change in the vertical and overhanging part of the large cornice in the Tyinstølen survey, but this would also have required calibration of local roughness parameters. Local surface roughness is generally not regarded as a main source of uncertainty in photogrammetric surface models, where errors often are locally correlated and roughness is removed by filtering and smoothing functions (James, Robson and Smith, 2017). Brief inspection of the dense point clouds confirmed a lack of small scale roughness, and introducing local interpolation through the M3C2 method were not regarded as beneficial compared to using the already interpolated 0.1 m DEMs.

DEM subtractions were performed with the Python package Rasterio⁴.

3.5.1 Level of detection (LoD)

Uncertainty in DEMs of difference can be treated by calculating the 'level of detection' (LoD) for a specified confidence level (Brasington et al., 2003; James, Robson and Smith, 2017). The LoD in vertical direction is given by

$$LoD = t * (\sigma_{z1}^2 + \sigma_{z2}^2)^{0.5}$$

where σ_{z1}^2 and σ_{z2}^2 represent the standard deviations of error of each DEM, and t determines the confidence level. For a t-distribution and 95% confidence level, $t = 1.96$. Changes below the LoD is classified as non-significant and can be discarded.

This method can be used with both uniform (Wheaton et al., 2010; Milan et al., 2011) and spatially varying (Lague et al., 2013; James, Robson and Smith, 2017) error values, and can be applied for three-dimensional change in comparison of point clouds. The latter was done by James, Robson and Smith (2017), introducing methods and tools to use tie point precisions in combination with the M3C2 method to calculate surface change with local confidence levels. With tie point precisions now directly available in the Metashape software, this method could have been simplified and adapted to be used with DEMs of difference. The development of such tools was, however, found to be beyond the scope of this work, and uniform LoDs were used to describe the significance of detected changes.

3.5.2 Snow depth calculation and validation

Snow depth (HS) DEMs of difference were computed by comparing snow surface DEMs to a LiDAR digital terrain model (DTM) representing the bare ground surface. The DTM

⁴<https://rasterio.readthedocs.io/en/stable/>

were obtained from the subproject 'Valdres 2013' of the nationwide high-resolution DTM (*Nasjonal digital høydemodell*, NDH⁵), and was downloaded as a geotiff with 0.25 m resolution. According to NDH specifications, the required absolute georeferenced accuracy of the given project is systematic error below 0.1 m and standard error on control points below 0.04 m.

Before comparison with 0.25 m DEMs, the DTM were re-projected to a matching grid. Snow depth maps were validated at CPs by comparison with snow depth measured manually with probe. Errors on individual CPs were calculated as $HS_{DoD} - HS_{CP}$, and total error as the RMSE. Throughout the thesis, the term 'snow depth' refers to the vertical height of the snowpack, denoted 'HS', as described in Fierz et al. (2009).

3.6 Measures of error, accuracy and precision

The terms 'error', 'accuracy' and 'precision' are within this work describing the following:

- Error: The difference between an estimated/modeled and a measured/true value, calculated by subtracting the measured from the estimated.
- Accuracy: How close a set of estimated/modeled values is to their measured/true value. Described by the mean error and the root-mean-squared error (RMSE).
- Precision: How close a set of estimated/modeled values is to their mean value. Described by the standard deviation (SD).

⁵www.hoydedata.no

4 Results

4.1 Field surveys

4.1.1 Survey data

A total of ten surveys was carried out on seven different field days between February 10th and March 19th 2019. Collected data is along with snow and weather conditions on the field days summarised in table 4.1.

Table 4.1: Overview of conducted surveys and collected data.

Date	Area	GCPs	CPs	Images	Snow surface	Weather/light
10.02	Tyinstølen	8	8	245	New snow	Clear, shades
10.02	Tyinstølen ¹	8	8	245	New snow	Clear, shades
11.02	Tyinstølen	8	15	247	New snow, wind-affected	Clear
15.02	Tyinstølen	8	15	289	Rain crust	Clear, minor shades
15.02	Tyinstølen	8	15	246	Rain crust	Clear, minor shades
18.02	Tyinstølen ¹	8	15	288	Crust/dry snow, wind-affected	Cloudy, flat light
18.02	Støl [*]	6	13	624	Crust/dry snow, wind-affected	Cloudy, flat light
18.03	Tyinstølen ¹	8	15	330	Crust/dry snow, wind-packed	Clear
19.03	Tyinstølen	8	15	320	Crust/dry snow, wind-packed	Clear
19.03	Lake Tyin	13	23	230	Crust/dry snow, wind-packed	Clear

¹ Rejected due to insufficient surface contrast or low image quality

One survey, on March 18th, was rejected before processing because the images were out of focus. The second survey on February 10th and both surveys on February 18th were rejected after initial photo alignment, as no tie points were identified in large parts of the survey areas due to lack of visible surface contrasts. Poorly contrasted areas were also present in the first survey on February 10th, which was processed nevertheless to evaluate the effect of sub-optimal light conditions on the final snow surface model. In total, six surveys were processed according to the steps described in section 3.3, of which five were of the Tyinstølen area and the last one were the test and validation survey at Lake Tyin. Orthophotos and distributions of GCPs and CPs from the surveys of Tyinstølen are shown in figure 4.1.

The different surveys are from now on referred to by the area name followed by survey date and, if necessary, survey number (e.g. Tyinstølen 150219_1).

Table 4.2: UAV and camera settings of processed surveys. Flying height represents the average distance normal to the ground within the survey area.

	Unit	Tyinstølen 100219	Tyinstølen 110219	Tyinstølen 150219_1	Tyinstølen 150219_2	Tyinstølen 190319	Lake Tyin 190319
Flying speed	<i>m/s</i>	8	8	7	8	7	7
Image overlap	%	86	86	86	86	86	86
Image sidelap	%	77	77	77	77	77	77
Survey range ¹	<i>m</i>	80	80	70	80	70	70
Survey range ²	<i>m</i>	79.3	71.8	74.3	81.2	77.9	72.5
GSD ¹	<i>cm/px</i>	2.82	2.82	2.47	2.82	2.47	2.47
GSD ²	<i>cm/px</i>	2.61	2.36	2.41	2.64	2.53	2.55
Aperture	<i>f-stop</i>	2.8	2.8	2.8	2.8	2.8	2.8
Focal length	<i>mm</i>	4.386	4.386	4.386	4.386	4.386	4.386
Focal length	<i>35mm eq.</i>	24	24	24	24	24	24
Shutter speed	<i>s</i>	1/1000- 1/2500	1/1000- 1/4000	1/2000- 1/4000	1/2500- 1/4000	1/3200- 1/5000	1/5000- 1/6000
ISO		100	110	100	100	100	110

¹ Planned

² Estimated by the Metashape software

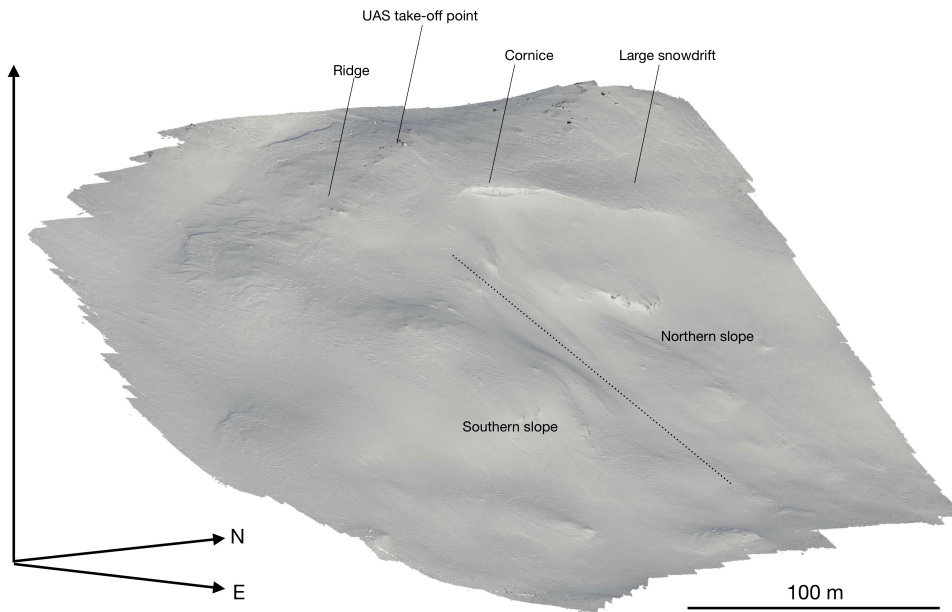


Figure 4.2: 3D visualisation of the dense point cloud from the Tyinstølen 190319 survey. Marked features is used for reference to locations within the survey area.

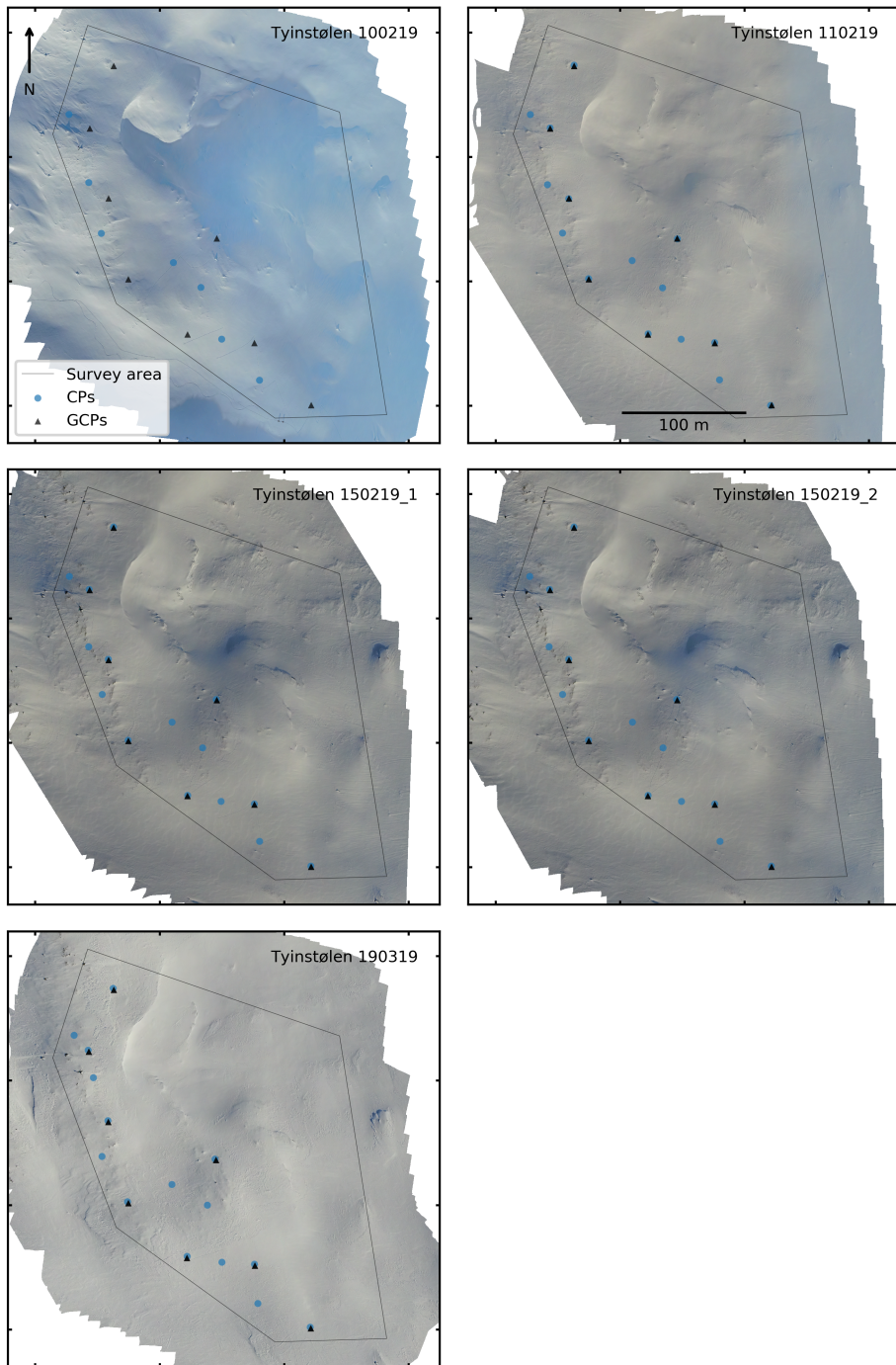


Figure 4.1: Orthophotos of snow covered terrain and recorded GCP and CP locations for the Tyinstølen surveys.

4.1.2 UAS and camera performance

Flight and camera details of the processed surveys are shown in table 4.2. Obtained average GSDs, as estimated by Metashape after processing, are between 2.36 and 2.64 cm/pixel. Camera exposure was controlled automatically by adjusting shutter speed and ISO. While ISO values are stable and low, shutter speeds are in the range 1/1000-1/6000 and vary largely both within and across surveys.

The recorded and estimated camera positions shown in figure 4.3 agree reasonably well with the planned flight paths in the horizontal direction. Vertically, however, two types of systematic differences between recorded and estimated positions can be observed. Firstly, the vertical differences increase with decreasing elevation, being around zero in the upper part of the flight and up to 8 meters in the bottom part. Secondly, the differences vary in some surveys in an alternating pattern between neighbouring strips.

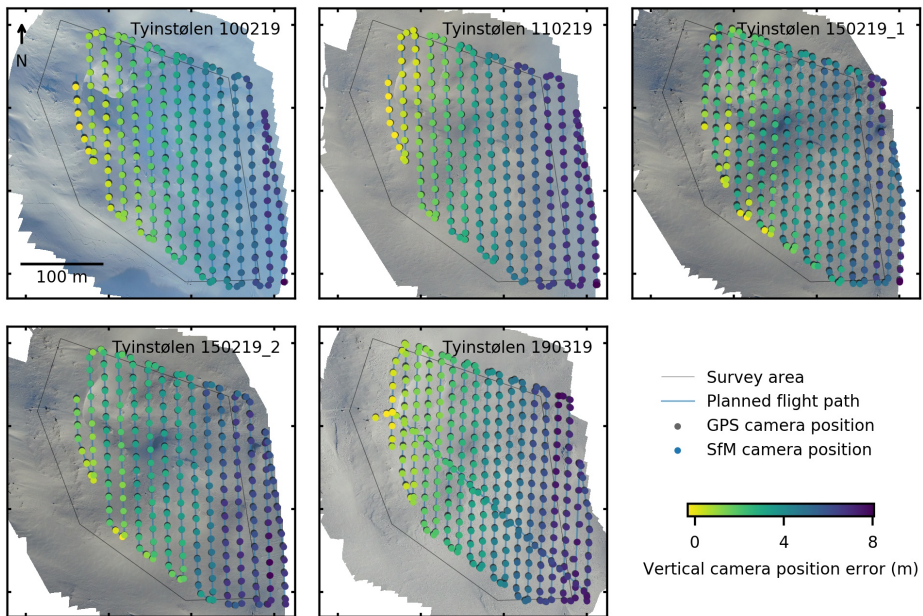


Figure 4.3: Planned flight path and measured and estimated camera positions for the Tyinstølen surveys. The grids were flown from top to bottom (west to east). Colored dots show the horizontal camera position estimated by the SfM processing and are plotted on over grey dots representing the position recorded by the UAS. The color represent the elevation error of recorded compared to estimated positions.

4.1.3 dGNSS measurement precision

The root-mean-squared standard deviations of 36 surveyed GCP and CP locations at Lake Tyin are given in table 4.3. Sub-centimetre precision were obtained in the horizontal directions, while vertical precision was slightly above 1 cm. The absolute accuracy of the positioning was not assessed, meaning that the relative precision of each survey is a potential source of error when comparing individually georeferenced models.

Table 4.3: GNSS precision obtained from 36 GCPs and CPs measured three times each with 20-30 minutes time intervals. The RMSE represents the root-mean-squared standard deviations.

	Unit	Easting	Northing	Elevation
RMSE	<i>m</i>	0.0069	0.0067	0.0108

4.2 Photogrammetric processing

4.2.1 Image observations and initial network calibration

An impression of the general image quality from surveys at Tyinstølen can be made from the orthophotos in figure 4.1. Both light conditions, snow depth and snow surface texture contribute to variable levels of contrast across the survey area. Image quality is further found to depend on camera and UAS performance. Examples of image blur and distortion are shown in figure 4.4.



Figure 4.4: Differences in image quality shown by zooming in on GCP target plates (see figure 3.5). Left: Well contrasted and little visible distortion, from near image center. Middle: Clear image blur, from near image center. Right: Significant image blur and distortion, from near image corner.

Table 4.4: Tie point numbers and accuracy measures for the initial network calibration steps. All steps were carried out with self-calibration of camera model B (see table 3.1), and marker accuracy set to 1.1 cm.

	Unit	Tyinstølen 100219	Tyinstølen 110219	Tyinstølen 150219_1	Tyinstølen 150219_2	Tyinstølen 190319
<i>1. Photo alignment</i>						
Tie points		171023	221424	245588	209396	142104
Image residuals	<i>px</i>	1.98	1.22	1.59	1.56	1.78
<i>2. Filtered sparse cloud, markers not included in bundle adjustment</i>						
Tie points		60816	90840	92720	88836	83857
Image residuals	<i>px</i>	1.74	0.89	1.10	1.49	1.62
Marker residuals	<i>px</i>	1.36	1.18	1.35	1.30	2.10
Marker errors	<i>m</i>	1.661	0.414	0.297	0.807	0.356
<i>3. Filtered sparse cloud, markers included in bundle adjustment</i>						
Image residuals	<i>px</i>	1.89	1.21	1.68	1.76	1.63
Marker residuals	<i>px</i>	1.70	1.02	1.98	1.45	2.11
Marker errors	<i>m</i>	0.184	0.765	0.353	0.337	0.238

Table 4.4 shows the number of tie point observations and obtained accuracies after photo alignment and initial self-calibrated bundle adjustments for the Tyinstølen surveys. Although the number of identified tie points vary greatly, the number of tie points left after filtering are similar for all surveys except Tyinstølen 100219. Reprojection errors were

reduced by the tie point filtering, but were increased again when markers were included in the bundle adjustment. Obtained marker errors are generally large, and vary from 0.18 to 0.77 m for bundle adjustments including markers. For two of the surveys, the marker error increased after inclusion of markers.

The spatial distribution of tie points and number of observations after filtering are shown in figure 4.5. All surveys show areas with reduced tie point density, while Tyinstølen 100219 and 110219 show a critical lack of tie point observations in parts of the survey area. The number of observations is generally between 3-10 for all surveys except Tyinstølen 190319. This survey included an additional strip of offset images and shows on average almost twice the number of observations per tie point.

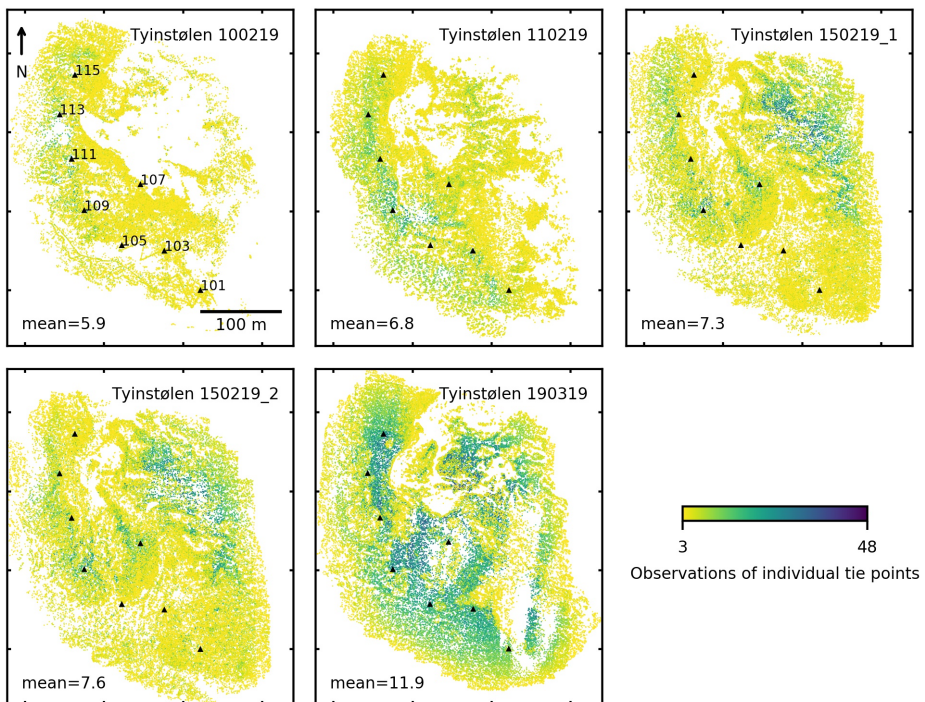


Figure 4.5: Tie point distributions for the Tyinstølen surveys. Colors represent the number of images each tie point was observed in, 'mean' is the average for the whole survey and 'n' is the total number of tie points.

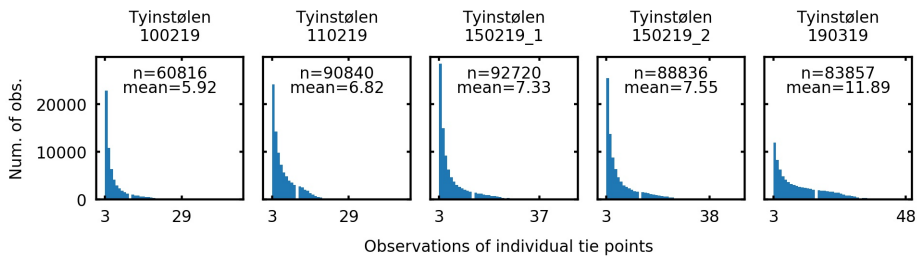


Figure 4.6: Observations of individual tie points for the Tyinstølen surveys.

4.2.2 Camera model calibration

The results of running self-calibrating bundle adjustments for camera model A, B and C for the Tyinstølen surveys are summarised in table 4.5. Compared to the initial calibration with camera model B, significantly improved accuracy were obtained only for the Tyinstølen 190319 survey. While image and marker residuals remain more or less unchanged across all calibrations, the marker error, representing the three-dimensional RMSE of all GCPs, drops from around 0.24 m to 0.04 m using camera model C.

An extended calibration analysis was then carried out for the Tyinstølen 190319 survey. Figure 4.7 shows the RMSE on GCPs and CPs obtained by self-calibrating bundle adjustments with varying marker accuracy settings run with and without rolling shutter compensation. The lowest errors is found for camera model C without rolling shutter compensation, where the RMSEs of both CPs (vertical) and GCPs (east, north, vertical) are stably below 0.1 m across all marker accuracies. The lowest ratio between CP error and vertical GCP error is found for marker accuracy set to 4 cm, where the RMSE is around 6 cm for both. The errors obtained by including rolling shutter compensation are similar across all camera models, and for high marker accuracies they are similar to the errors obtained with camera model C without the compensation.

Using the sparse point cloud obtained with camera model C, marker accuracy 4 cm and no rolling shutter compensation as reference, it was investigated how changing these parameters affected overall surface geometry. As shown in figure 4.8, enabling rolling shutter compensation cause large tie point elevation changes, with magnitudes increasing with distance away from the region covered by GCPs. Similar magnitudes and spatial distribution were also found for changes in horizontal direction. Comparing the compensated sparse cloud with the DTM (bare ground), tie points were found both well below ground level and horizontally displaced at common surface features in the region with greatest change.

Consequently, the self-calibrated camera model C, without rolling shutter compensation and with marker accuracy of 4 cm, was regarded optimal for the Tyinstølen 190319 survey. Processing the other surveys with the same camera model and settings gave marker errors of 0.07-0.083 m across all surveys, and image and marker residuals in the range of 1.62-2.2 pixels (see table 4.5). As the results were significantly better than what was obtained with self-calibration only, these settings were used for further processing.

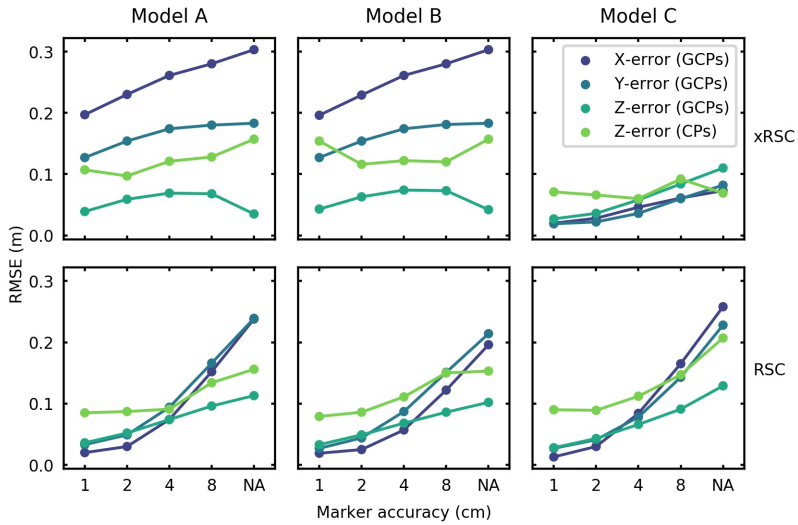


Figure 4.7: RMSE on GCPs and CPs obtained by self-calibration of camera models A, B and C for the Tyinstølen 190319 survey, across a range of marker accuracies and with rolling shutter compensation enabled/disabled (RSC/xRSC). CP errors represent the vertical distance between CP coordinates and local averages of the sparse point cloud, calculated with M3C2. Marker accuracy 'NA' represent calibrations where markers were excluded from bundle adjustments and only used for scaling and orientation.

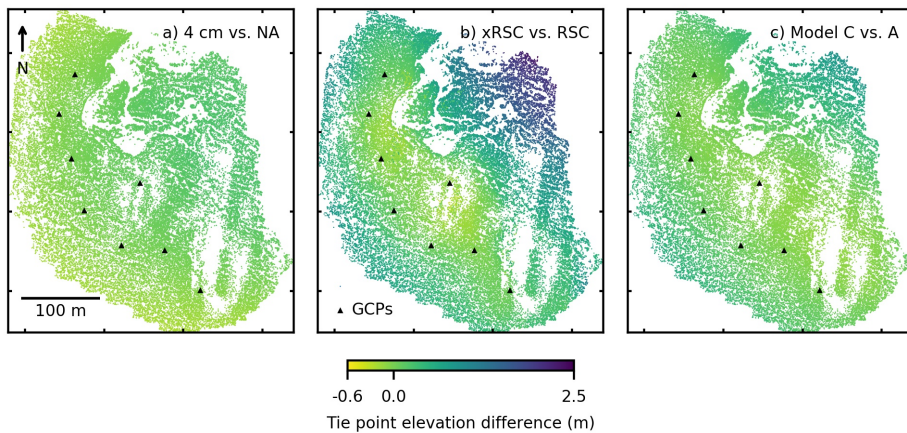


Figure 4.8: Effects on tie point elevations of a) excluding markers from bundle adjustment, b) enabling rolling shutter compensation and c) changing camera model, using the sparse cloud obtained with camera model C, marker accuracy 4 cm and no rolling shutter compensation as reference.

Table 4.5: Precisions and camera model parameter values f (focal length) and C_x , C_y (principal point) obtained by self-calibration of model A, B, and C for each survey, and by self-calibration of model C for Tyinstølen 190319 and using this as a fixed model for the other surveys. For the final calibration, marker accuracy were set to the optimal value (4 cm) found by the error analysis shown in figure 4.9.

	Unit	Tyinstølen 100219	Tyinstølen 110219	Tyinstølen 150219_1	Tyinstølen 150219_2	Tyinstølen 190319
<i>Camera model A, self-calibrated with marker accuracy = 0.011 m</i>						
Image residuals	px		1.21	1.69	1.77	1.64
Marker residuals	px		1.01	1.97	1.46	2.12
Marker errors (xyz)	m		0.77	0.35	0.34	0.24
f	px		2908	2954	3004	2845
C_x	px		-137	-81	-76	-9
C_y	px		-455	-242	-230	3
<i>Camera model B, self-calibrated with marker accuracy = 0.011 m</i>						
Image residuals	px	1.89	1.21	1.68	1.76	1.63
Marker residuals	px	1.70	1.02	1.98	1.45	2.11
Marker errors (xyz)	m	0.184	0.765	0.353	0.337	0.238
f	px	2928	2907	2953	3004	2847
C_x	px	-83	-135	-78	-74	-9
C_y	px	-141	-452	-241	-230	3
<i>Camera model C, self-calibrated with marker accuracy = 0.011 m</i>						
Image residuals	px	1.83	1.11	1.54	1.64	1.62
Marker residuals	px	1.62	0.92	1.68	1.26	2.10
Marker errors (xyz)	m	0.191	0.626	0.427	0.322	0.038
f	px	3004	2970	2987	3039	2840
C_x	px	-16	-94	-41	-35	-27
C_y	px	-200	-485	-317	-248	11
<i>Camera model C, self-calibrated for Tyinstølen 190319 with marker accuracy = 0.04 m (final calibration)</i>						
Image residuals	px	2.00	1.83	1.95	2.01	1.62
Marker residuals	px	1.79	1.80	2.20	2.00	2.10
Marker errors (xyz)	m	0.070	0.083	0.075	0.076	0.082
f	px	2840	2840	2840	2840	2840
C_x	px	-24	-24	-24	-24	-24
C_y	px	13	13	13	13	13

4.2.3 GCP analysis

Figure 4.9 shows the errors on individual GCPs obtained by bundle adjustments with varying GCP configurations. Similar patterns of relative GCP performance can be found, especially across the last three surveys. Disabled GCPs are associated with larger errors and larger variation than enabled ones, and the largest errors are found for GCP no. 101, 107 and 115 (for location see figure 4.10). Vertical errors are clearly positive for GCP no. 101 and 115, clearly negative for no. 107 and a tendency towards negative errors is found among the rest. The difference between disabled and enabled errors on GCP no. 101 is relatively large, indicating that this GCP has a particularly large influence on surface geometry.

The sensitivity of overall surface geometry to varying GCP configurations is illustrated by variations in tie point elevation in figure 4.10. Variations are smallest in the centre of the regions covered by GCPs, from where they gradually increase. The largest variations are therefore found towards the eastern margin of the survey areas, where standard deviations at most are up to 12.5 cm. Tie point elevations with all eight GCPs enabled were found to be close to the mean tie point elevations across all surveys, and this configuration were kept for the final processing.

Similar vertical and horizontal (plot in appendix B) variation magnitudes and spatial distribution are found for all surveys except Tyinstølen 110219, where vertical variations are significantly smaller. Vertical errors on GCPs are equivalently small for this survey, which they also are for the Tyinstølen 100219 survey. A large proportion of the tie points in both of these surveys is concentrated around the region covered by GCPs, which might have affected the relative influence of GCPs during bundle adjustments.

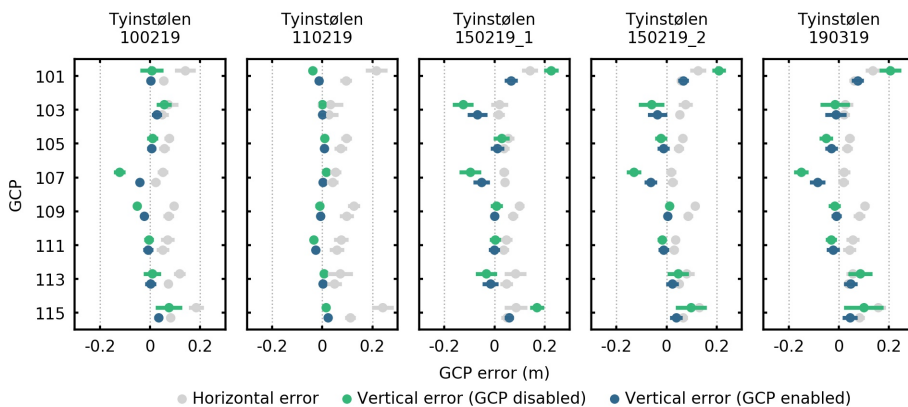


Figure 4.9: Errors on individual GCPs for all possible configurations of 6-8 enabled GCPs ($n=37$), shown by the mean (dots) and standard deviation (bars). Colored symbols represent vertical errors for enabled and disabled GCPs, respectively, and the aligned grey symbols represent their corresponding horizontal errors (absolute values). GCP locations are shown in figure 4.10.

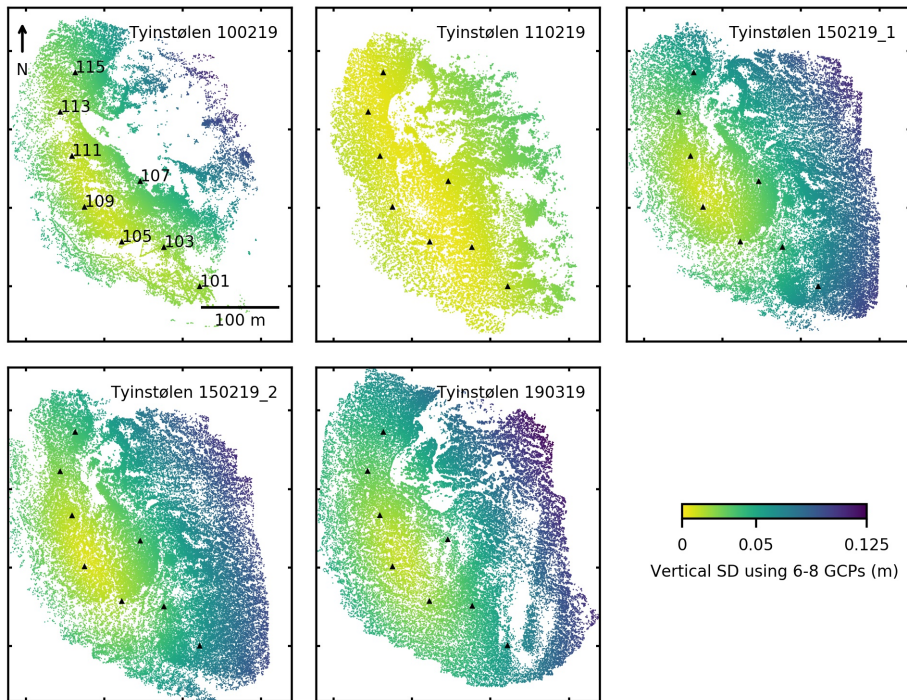


Figure 4.10: Tie point elevations for all possible configurations of 6-8 enabled GCPs ($n=37$), shown by the standard deviation on each point. Black symbols show GCP locations (point IDs in first frame).

4.3 DEM validation

Measures of accuracy and precision for the final Tyinstølen snow surface DEMs are listed in table 4.6. The dense point clouds consist of 12.6-13.9 million points and cover areas estimated to 0.104-0.113 km², giving point densities in the range of 113 to 133 points/m². It should be noted that the dense point clouds include noisy and geometrically distorted areas of varying extent around the edges, which means that the useful parts of the models are smaller.

Table 4.6: Measures of accuracy and precision for the final Tyinstølen snow surface DEMs.

	Unit	Tyinstølen 100219	Tyinstølen 110219	Tyinstølen 150219_1	Tyinstølen 150219_2	Tyinstølen 190319
Dense points		13447063	13883544	13861907	12647570	13495756
Area covered	<i>m</i> ²	0.112	0.104	0.107	0.112	0.113
Average point density	<i>points/m</i> ²	120	133	130	113	119
<i>Reprojection errors (RMSE)</i>						
Tie points	<i>px</i>	2.00	1.83	1.95	2.01	1.62
Markers	<i>px</i>	1.79	1.80	2.20	2.00	2.10
<i>Tie point precisions (mean standard deviations)</i>						
X	<i>m</i>	0.031	0.022	0.032	0.035	0.021
Y	<i>m</i>	0.026	0.020	0.027	0.029	0.020
Z	<i>m</i>	0.079	0.056	0.083	0.090	0.045
<i>GCP errors (RMSE)</i>						
X	<i>m</i>	0.039	0.059	0.043	0.040	0.046
Y	<i>m</i>	0.051	0.056	0.029	0.043	0.036
Z	<i>m</i>	0.028	0.015	0.054	0.048	0.058
Total (XYZ)	<i>m</i>	0.070	0.083	0.075	0.076	0.082
<i>CP errors (RMSE, Z)</i>						
DEM 0.25 m	<i>m</i>	0.068	0.064	0.036	0.048	0.065
DEM 0.10 m	<i>m</i>	0.044	0.062	0.042	0.037	0.058
Dense cloud	<i>m</i>	0.046	0.057	0.033	0.035	0.059
CP/GCP error ratio ¹		1.6	4.2	0.8	0.8	1.0
Relative CP accuracy ²		1/1800	1/1151	1/1784	1/2182	1/1352

¹ CP error (0.10 m DEM) divided by GCP Z error

² CP error (0.10 m DEM) divided by survey range

4.3.1 Photogrammetric precision

RMS reprojection errors of image observations and markers for each survey, as given by the Metashape software, are found between 1.62 and 2.1 pixels (table 4.6). As seen by the RMS reprojection errors of individual images in figure 4.12, local variations are large. This variation is better examined in the reprojection error on individual tie points, as shown in figure 4.14 and 4.13, which is clearly spatially dependent. The highest magnitudes are observed in distinct regions mainly located in or close to areas of lower tie point density. Such regions are especially seen in the Tyinstølen 150219_1 and 150219_2 surveys, in which magnitudes generally exceed 4 pixels. With ground sampling distances of around 2.5 cm/pixel, this correspond to distances of at least 10 cm in the surface coordinate system. Some variation due to systematic errors related to the camera calibration is also indicated by barely visible linear patterns. The distribution of reprojection errors within the image plane (figure 4.11) show that repeated patterns of mis- or uncorrected distortion both in the corners and in central parts of the image plane are present in the imagery.

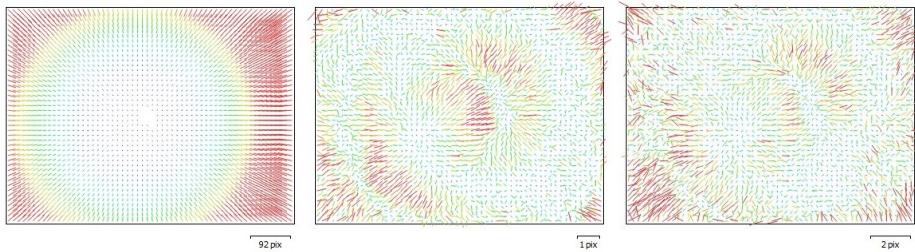


Figure 4.11: Left: Lens distortion correction vectors given by the camera calibration model used for the Tyinstølen surveys. Middle, right: Mean RMS reprojection errors based on location on the image plane for the Tyinstølen 190319 and 150219_1 surveys.

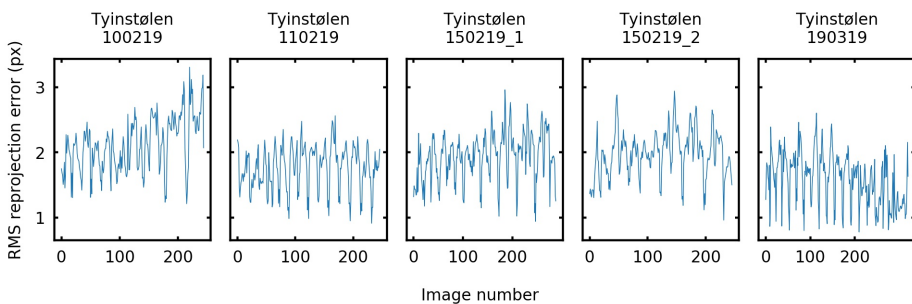


Figure 4.12: RMS reprojection errors on individual images for the Tyinstølen surveys.

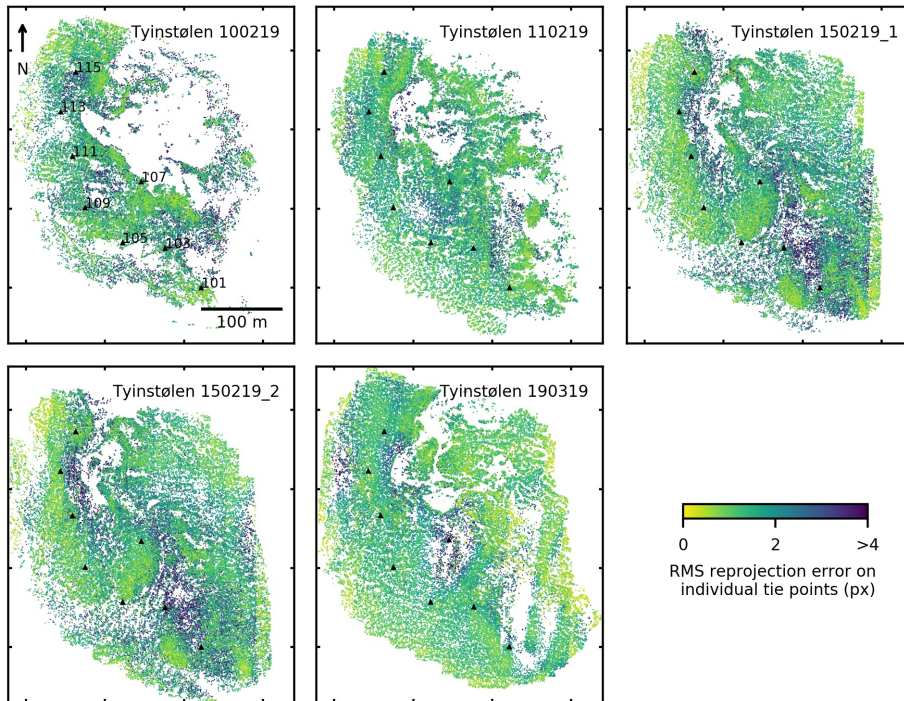


Figure 4.13: Spatial distribution of RMS reprojection errors on individual tie points. The total RMSE differs slightly from the total reprojection error given in table 4.6, which is given by the Metashape software and represents the averaged RMS reprojection error of all images. The quantity that is minimized during bundle adjustment is a normalized version of the reprojection error, scaled to the size of the associated key point (Agisoft, 2018a).

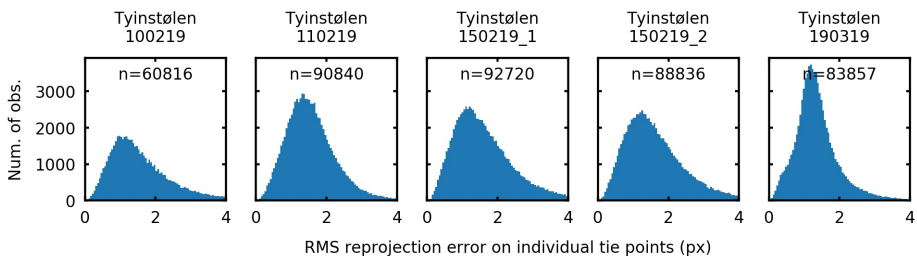


Figure 4.14: Observations of RMS reprojection errors on individual tie points for the Tyinstølen surveys.

Total tie point precisions for each survey, represented by the mean standard deviations, range from 5.9 to 13.1 cm in vertical direction and from 2 to 3.5 cm in horizontal directions (for distributions see figure 4.15). Spatial distributions of vertical tie point precision are shown in figure 4.16. The precision vary mainly from areas of high tie point density (high precision) to low tie point density (low precision), similar to the variations seen for reprojection errors. The same pattern is found for horizontal tie point precision (see appendix C). Vertical precision magnitudes exceeding 30 cm are found in the regions with lowest precision, and on scattered individual tie points. The Tyinstølen 150219_1 and Tyinstølen 150219_2 surveys suffer, despite well distributed tie points, from generally low precisions, while Tyinstølen 190319 shows significantly higher precisions compared to the rest of the surveys.

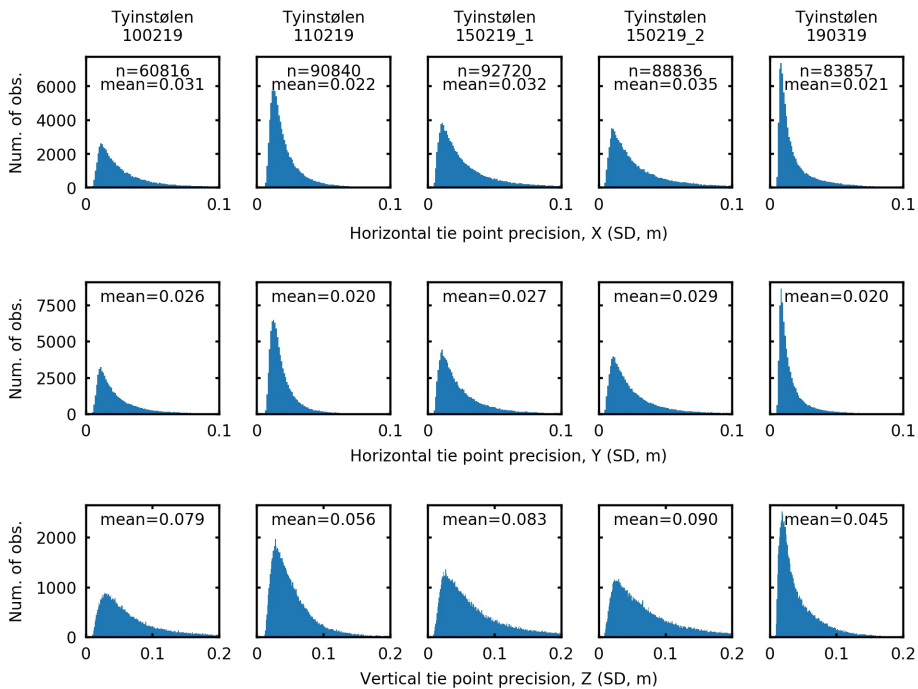


Figure 4.15: Observations of tie point precision given by their components in east-west (X), north-south (Y) and vertical (Z) direction.

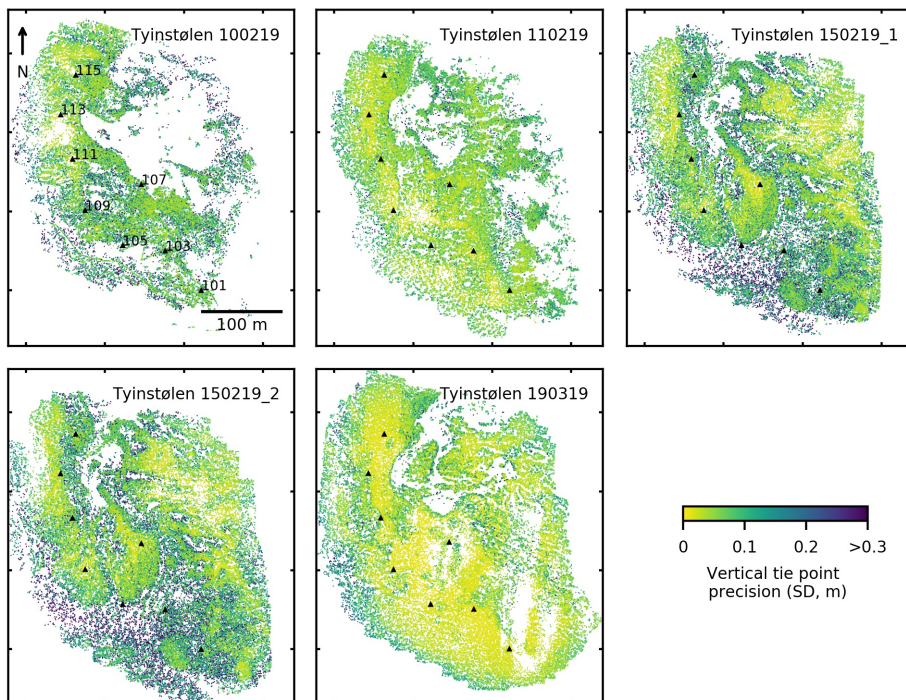


Figure 4.16: Spatial distribution of vertical tie point precisions. Point precision is shown by the standard deviation of each tie point, and the RMS represents the root-mean-squared standard deviations for each survey.

4.3.2 Georeferencing accuracy

Total (three-dimensional) RMSEs on GCPs are between 7 and 8.3 cm for the Tyinstølen surveys. The components in each direction have relatively equal magnitudes, of which vertical errors vary the most and range from 1.5 to 5.8 cm. RMSEs on CPs vary slightly depending on which DEM type and resolution they are calculated, but all values are found between 3.3 and 6.8 cm. Errors on CPs give RMSE/range ratios between 1/1151 and 1/2182 using the average survey ranges estimated by the Metashape software.

As shown in figure 4.17, most of the vertical errors of individual GCPs and CPs are less than ± 10 cm. The coarsest 0.25 m DEMs show overall slightly larger and more outspread errors, but the differences to the 0.1 m DEMs and the dense point clouds are small. CP errors are largely positive, i.e. model elevations tend to be exaggerated, for the Tyinstølen 110219 and 190319 surveys, while no clear trend is visible for the remaining surveys.

Spatial error patterns can be seen in figure ?? . Horizontal errors on GCPs are similarly distributed across all surveys, regarding both directions and relative magnitudes. In correspondence with findings in the GCP analysis (figure 4.9), vertical error on GCPs 101 and 115 tend to be positive, while the error on GCP 107 tend to be negative. The latter location is also associated with generally large CP errors.

4.3.3 Georeferencing precision

Uncertainties related to the scale and orientation of models after georeferencing can be illustrated with the results of the GCP analysis (section 4.2.3). In summary, they show that the precision decreases with distance away from the centre of the region covered by GCPs, and that displacements of up to 10-20 cm in both horizontal and vertical direction can be expected as a result of small variations in the GCP configuration. The exception is the Tyinstølen 110219 survey, which is found much less sensitive to such variations.

Vertical CP/GCP error ratio of 4.2, mainly caused by very low GCP error, for the Tyinstølen 110219 survey (table 4.6) indicates that the shape of this DEM is strongly influenced by implementation of GCPs. Such high ratios is not found for any of the other surveys, although the Tyinstølen 100219 survey also show unexpectedly low vertical errors on GCPs. Spatial distributions of vertical error (figure ??) show some local disagreements between GCPs and CPs, which may indicate deformations that is not reflected in the overall RMSE ratio.

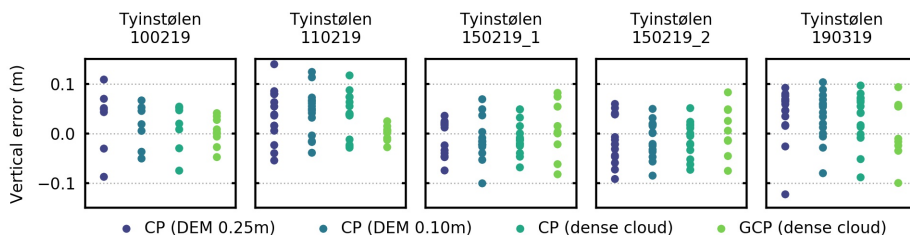


Figure 4.17: Vertical errors on individual GCPs and CPs, showing the different CP errors obtained for dense point clouds and DEMs of different resolution.

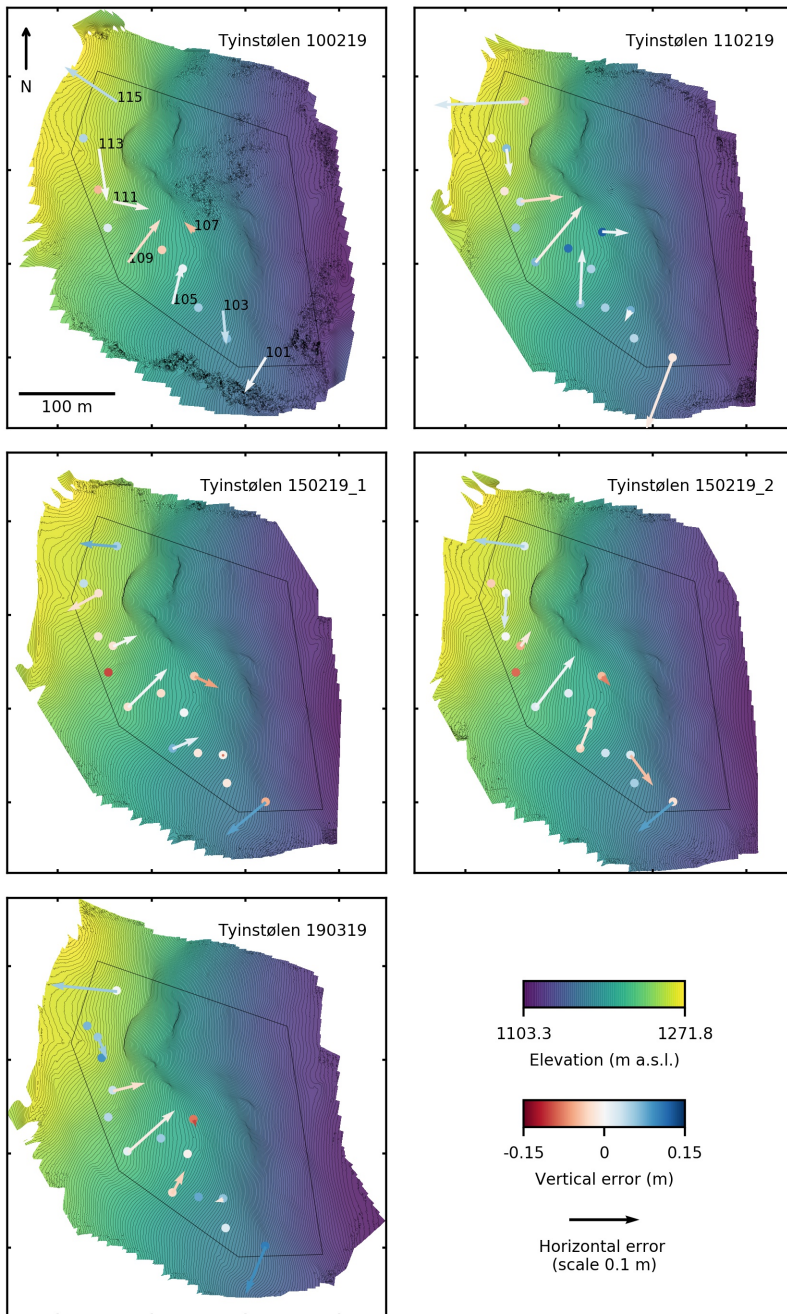


Figure 4.18: Spatial distribution of errors on GCPs and CPs shown on 0.10 m resolution DEMs with 1 m contourlines. Colored arrows represent GCP errors, where the vertical error component is shown by the color and the horizontal component by the arrow length and direction. Colored dots show the vertical errors on CPs. A similar plot of 0.25 m DEMs and the corresponding errors can be found in appendix D.

4.3.4 Systematic errors

The repeating pattern of relatively large and equally directed horizontal errors on GCPs shown in figure 4.18, indicates that significant systematic errors are present in all DEMs of the Tyinstølen survey area.

The presence of such errors is even more clear in the DEM of the Lake Tyin survey area, of which the surface elevation distribution and corresponding GCP and CP errors are presented in figure 4.19. Here, a slight upward bending of the surface towards the western and eastern corners is visible, causing elevation differences of up to 10-20 cm. Errors on CPs and GCPs confirm this model-scale deformation, being overall negative along a central north-south axis and positive towards the eastern and western corners.

In addition to the model-scale bending, local elevation differences are visible both across and along the flight strip direction. Strips were directed along the longest axis of the survey area and the camera top was headed towards northwest. The resulting elevation differences appear as linear patterns with increasing clarity towards the edges.

Although the systematic error patterns seen in the Lake Tyin DEM can not be directly transferred to Tyinstølen DEMs, similar flight grids and average ranges make it likely that similar systematic errors, with the same distribution relative to the flight strip and camera direction, exist.

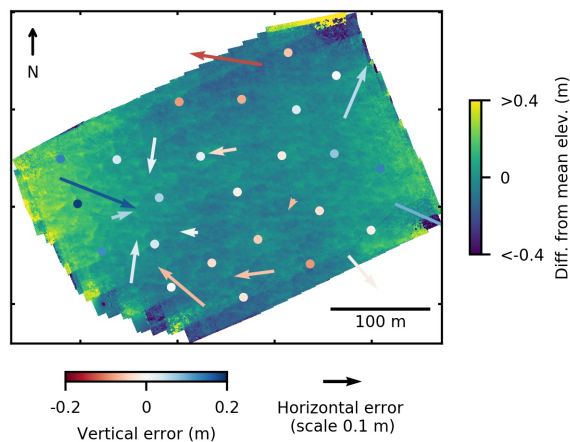


Figure 4.19: Systematic error patterns visible in DEM of the Lake Tyin survey area. The DEM was produced using the same camera calibration model and accuracy settings as for the Tyinstølen DEMs. Surface elevations are plotted by their deviation from the mean surface elevation. Colored dots represent the vertical error on CPs and arrows show the GCP errors, the vertical component being shown by the color and the horizontal component by the arrow length and direction.

4.4 Snow depth maps

Snow depth maps representing the difference between snow surface DEMs and the bare-ground DTM are shown in figure 4.21. For all the Tyinstølen surveys combined (67 CPs in total), the mean error on CPs is -1.1 cm and the RMSE is 10.3 cm. Errors for each survey is given in table 4.7, while snow depth observations within the survey area is summarised in figure 4.20. The latter show a slightly increasing average snow depth during the survey period. Negative minimum snow depth values are present for all surveys, and while HS values from Tyinstølen 100219 suffer from noise in the snow surface DEM, the minimum values ranging from -0.1 to -0.37 in the other surveys represent errors related to the accuracy and precision of the DEM, DTM or both.

Table 4.7: Snow depth errors on CPs representing the difference between modeled snow depth and manual measurements with probe.

	Unit	Tyinstølen 100219	Tyinstølen 110219	Tyinstølen 150219_1	Tyinstølen 150219_2	Tyinstølen 190319
Mean error	<i>m</i>	-0.011	0.011	-0.019	-0.021	-0.016
RMSE	<i>m</i>	0.052	0.093	0.101	0.106	0.127

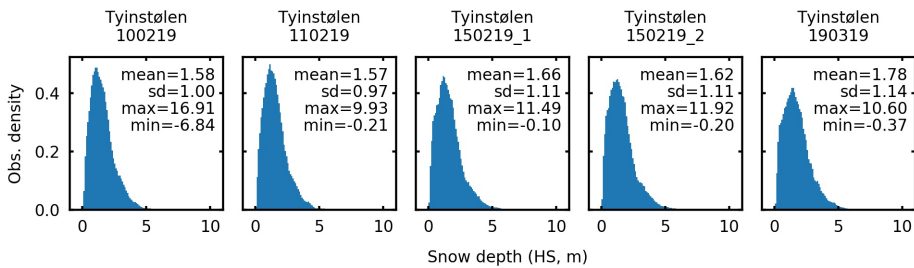


Figure 4.20: Snow depth observations within the survey area, based on the snow depth maps with 0.25 m resolution. The statistics from Tyinstølen 100219 include areas with significant noise in the snow surface DEM, explaining the high max and low min values.

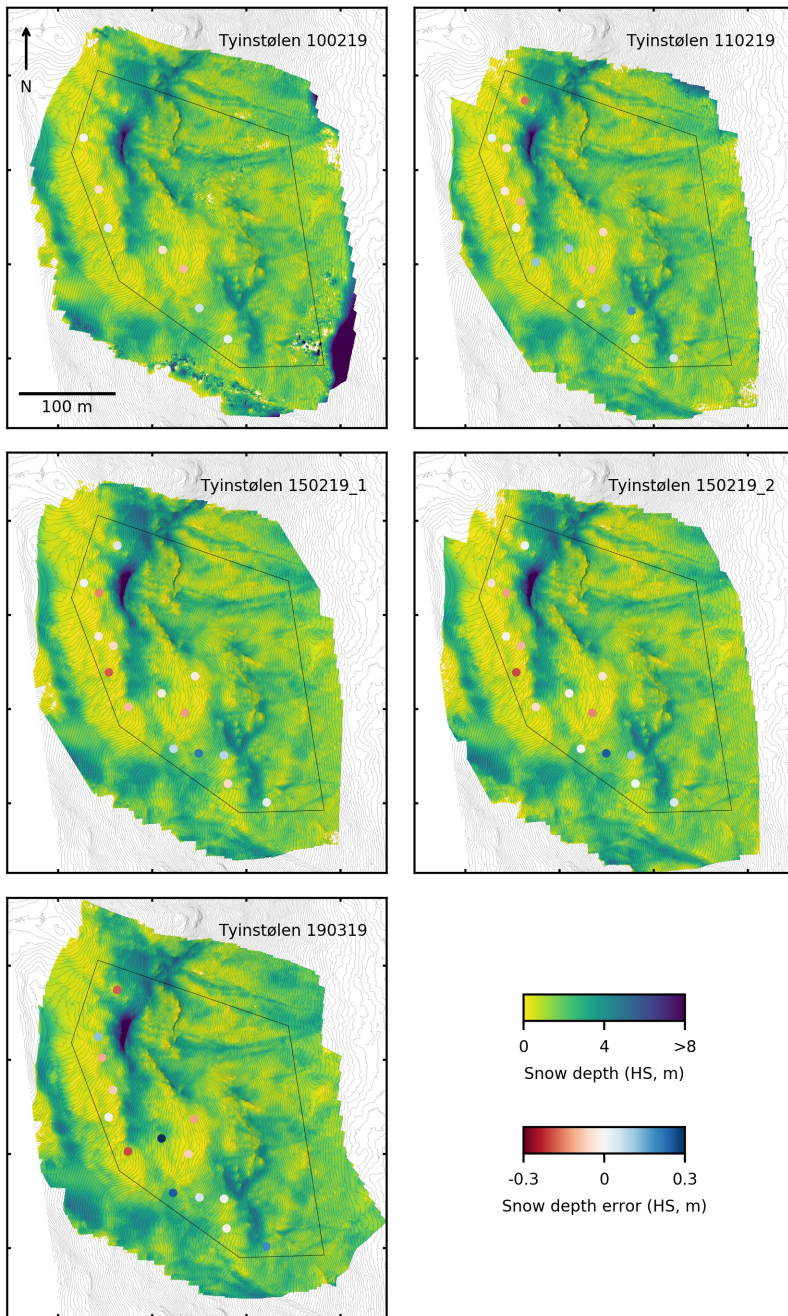


Figure 4.21: Snow depth (HS) maps with 0.25 m resolution of the Tyinstølen area, with colored dots representing the error of modelled snow depth compared to probe measurements. The snow-free terrain is shown by 1 m contourlines based on the DTM, and the polygon show the defined survey area from which the snow depth observation distributions in figure 4.20 are collected.

4.5 Snow depth change detection

Four pairs of DEMs from Tyinstølen, representing the snow cover at the beginning and the end of four different time periods, were compared and analysed for snow depth changes. The DEM pairs and the expected scale of change for each period are given in table 4.8.

Table 4.8: Periods analysed for snow depth changes. Scale of change represents the maximum expected snow depth change based on weather data and field observations.

Period	Reference DSM	Compared DSM	Days	Scale of change
P1	Tyinstølen 100219	Tyinstølen 110219	1	< 50 cm
P2	Tyinstølen 150219_1	Tyinstølen 150219_2	0	No change
P3	Tyinstølen 110219	Tyinstølen 150219_2	4	> 1 m
P4	Tyinstølen 150219_2	Tyinstølen 190319	32	> 1 m

4.5.1 Minimum level of detection

The minimum level of detection for each period depends on the accuracy of the compared DEMs and is shown in table 4.9. Lower errors on CPs were found for higher DEM resolutions, hence is the original dense point clouds giving the lowest levels of detection, ranging from 9.4 to 15.9 cm, and the 0.25 m resolution DEMs the highest, ranging from 11.7 to 19.6 cm.

Table 4.9: Level of detection, $LoD_{95\%}$, for each of the analysed periods.

	Unit	P1	P2	P3	P4
DEM 0.25 m	<i>m</i>	0.150	0.117	0.196	0.147
DEM 0.10 m	<i>m</i>	0.119	0.109	0.166	0.150
Dense cloud	<i>m</i>	0.103	0.094	0.159	0.132

4.5.2 Weather data

Figure 4.22 and 4.23 show temperature, precipitation, wind speed and wind direction measured at the Langøddin avalanche tower during the analysed periods. The tower is situated on top a steep, east-facing slope about 2 km south of the Tyinstølen survey area, and the measurements are assumed to be fairly representative of the weather in the survey area.

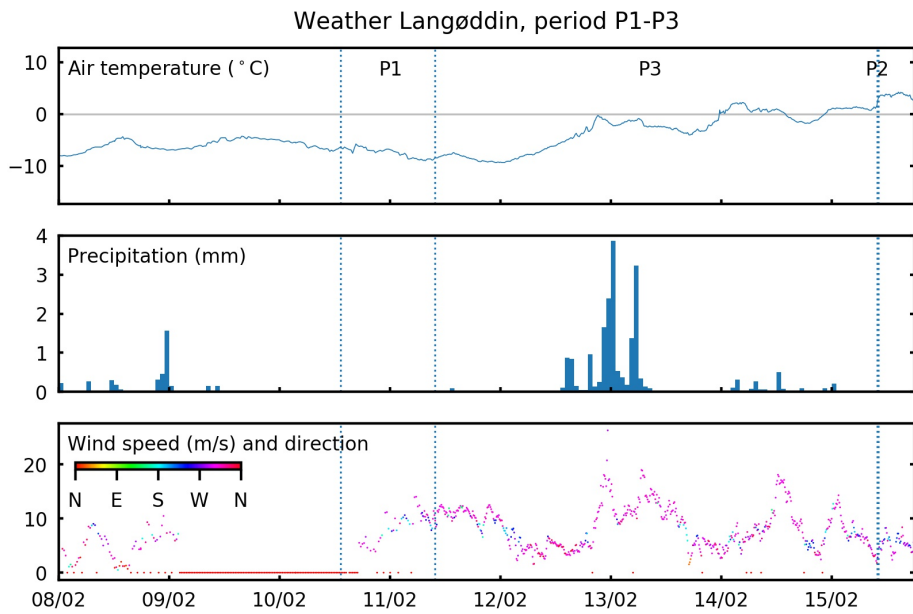


Figure 4.22: Weather during period P1-P3 at Langøddin avalanche tower. Air temperature, wind speed and wind direction show observations with 10 min resolution, while precipitation is summarised per hour. Stippled lines represent the times when surveys were conducted. (Data: Wyssen Norge AS)

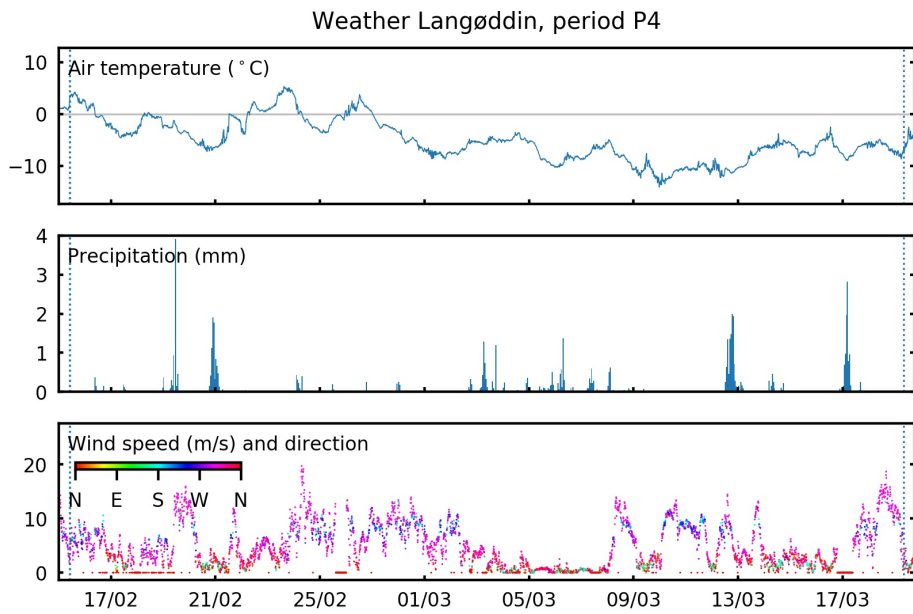


Figure 4.23: Weather during period P4 at Langøddin avalanche tower. Air temperature, wind speed and wind direction is shown by observations with 10 min resolution, while precipitation is summarised per hour. Stippled lines represent the times when surveys were conducted. (Data: Wyssen Norge AS)

4.5.3 DEMs of difference (DoDs)

Given the expected scales of change and the minimum levels of detection, little and no significant change were expected for period P1 and P2, while extensive significant change were expected for period P3 and P4. Detected changes within the survey area are summarised in figure 4.24. Change exceeding the level of detection is mainly found in period P3 and P4. Almost no significant change is detected in period P2, while some change appear as significant in period P1.

As shown in figure 4.25, a large part of the significant change detected in period P1 is caused by noise in the Tyinstølen 100219 DEM. The snow depth reduction found between the largest area of noise and the northern survey margin, may also be regarded as unlikely based on the time period and weather conditions. The last type of significant change indicates deposition in steep, east facing areas, which appear as realistic changes. This is supported by looking at the non-significant change, where continuous areas of slight erosion and deposition seem to be related to terrain rather than systematic errors.

Detected change in period P2 appear on the other hand to be controlled by systematic errors. This is indicated by the linear change variations in the direction of the flight strips. Some of the related change also exceeds the level of detection and is shown as significant, although most change within the survey area is not.

The main significant change detected during period P3 is deposition around the snowdrift and cornice on top of the northern slope, and a general snow depth reduction in the lower, eastern parts of the survey area (figure 4.26). A small region of snow depth increase at the bottom of the northern slope, outside of the survey area, is also detected as significant. For period P4, the significant change indicates a general snow depth increase in all concave terrain formations, with the largest increase found along a small depression west of the survey area. A reduction of snow depth is also found on top of the snowdrift/cornice that were growing in period P3. None of these DEMs of difference show signs of systematic errors.

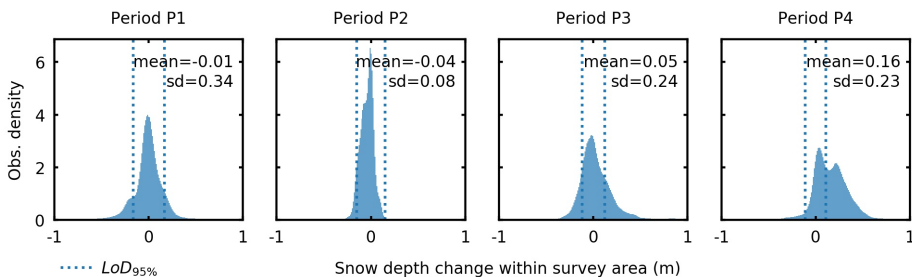


Figure 4.24: Observations of snow depth change within the survey area, based on 0.1 m resolution DEMs. The vertical lines show the minimum level of detection, and observations outside these represent significant change.

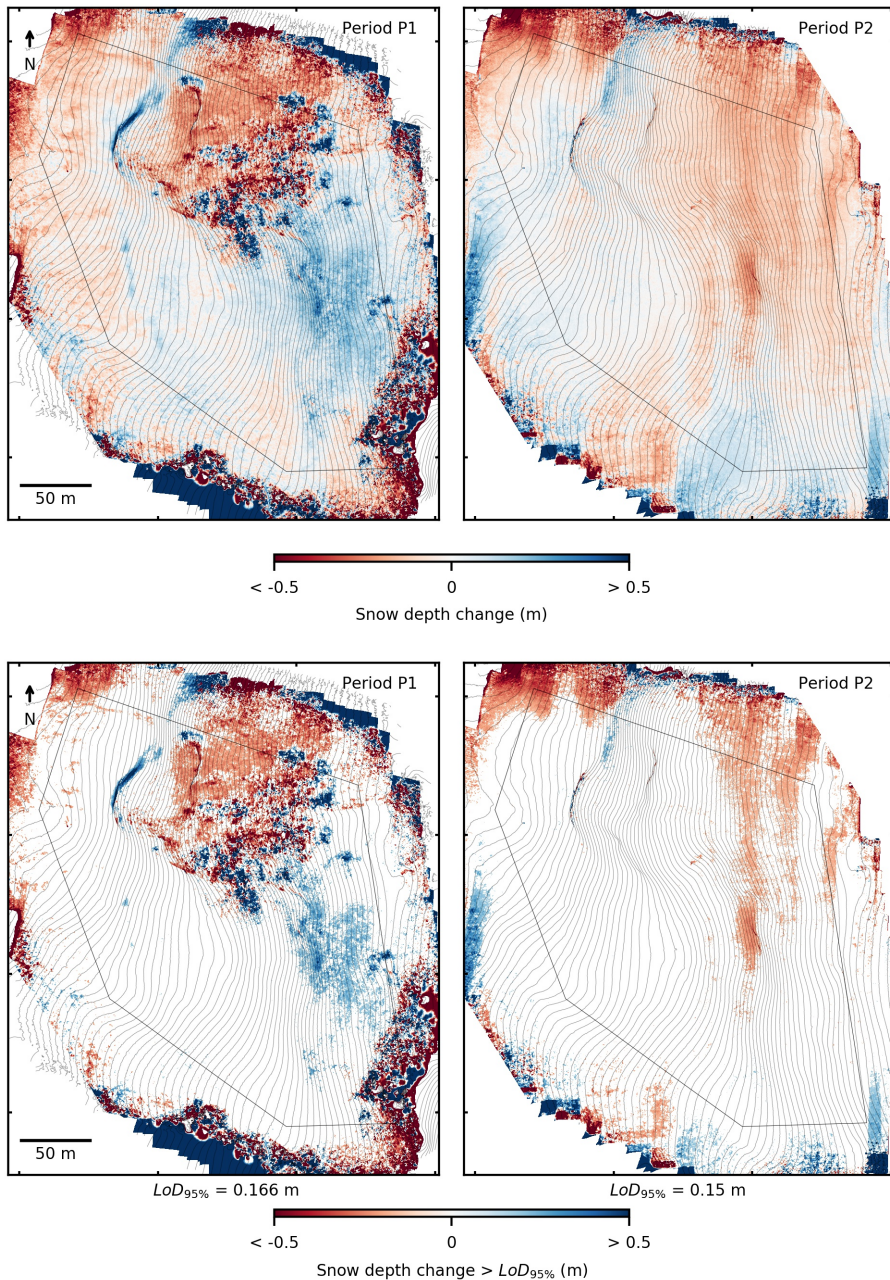


Figure 4.25: 0.1 m resolution DEMs of difference representing detected snow depth changes during period P1 and P2, positive values (blue color) representing increased snow depth. Upper plots show the full range of detected change, while lower plots show significant change. Contour lines with 2 m intervals from the reference DEMs represent the snow surface at the beginning of each period.

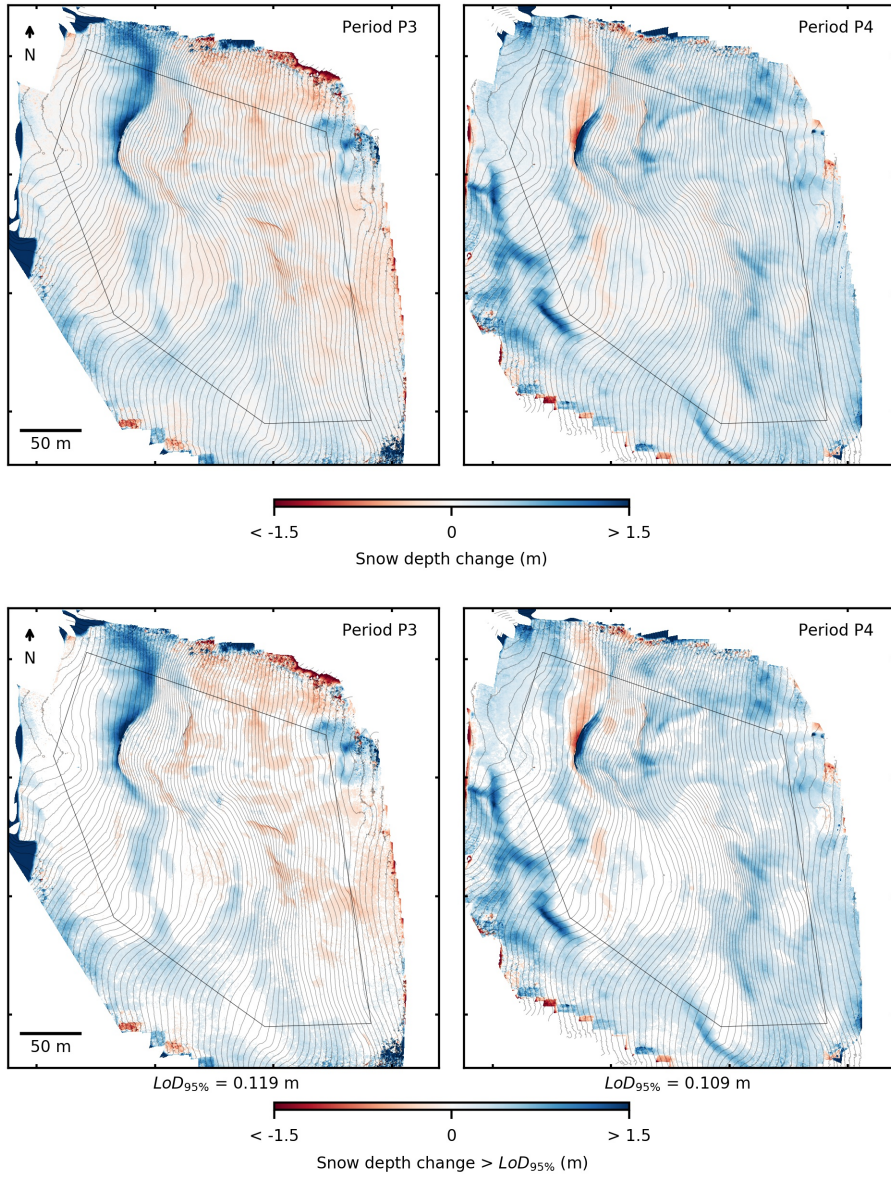


Figure 4.26: 0.1 m resolution DEMs of difference representing detected snow depth changes during period P3 and P4, positive values (blue color) representing increased snow depth. Upper plots show the full range of detected change, while lower plots show significant change. Contour lines with 2 m intervals from the reference DEMs represent the snow surface at the beginning of each period.

5 Discussion

5.1 DEM precision and accuracy

5.1.1 Photogrammetric precision

Well distributed, good quality tie point observations and a precise calibration of camera parameters, are key elements for obtaining a precise internal photogrammetric network. The less GCPs that are used to control the final surface geometry, the more important the reliability of the internal network is, making the photogrammetric precision a critical factor in this study. Initial processing stages revealed, however, that a useful self-calibrated camera model only could be achieved for one of the surveys, Tyinstølen 190319. The identified tie points were also unevenly distributed both within and across surveys, and associated with highly varying reprojection errors.

The main reason behind the erroneous self-calibrations is believed to be near-parallel and equally oriented image sets, not providing the necessary viewing angles for the camera model and poses to be unambiguously defined. Applying the self-calibrated camera model from Tyinstølen 190319 as a fixed model gave similar precision and accuracy magnitudes across all of the Tyinstølen surveys. This shows that a pre-calibrated camera model may pose a useful alternative when limitations of the image set make correct self-calibration impossible. This is discussed also by James, Robson, d'Oleire Oltmanns and Niethammer (2017), suggesting that a pre-calibrated camera model should be used if the GCP distribution is sparse - given that the camera model can be precisely determined.

Overall reprojection errors do not seem to be commonly reported in geomorphological studies, but compared to the case studies by James, Robson, d'Oleire Oltmanns and Niethammer (2017) (0.69-0.88 pixels) and recommendations for other photogrammetric software (Pix4D (2019), maximum 1 pixel), overall errors of 1.6 to 2.1 pixels are relatively high. Although the Tyinstølen 190319 survey, which the camera model was calibrated for, gave the lowest errors, these are also high, indicating a sub-optimal calibration in the first place. Furthermore are the irregular distributions of reprojection errors in the image planes (figure 4.11), and the slight linear patterns among tie point reprojection errors (figure 4.13), indicating that uncorrected lens distortion is likely to have contributed to generally high reprojection errors.

Consumer grade, wide angle cameras are generally associated with significant irregular lens distortion patterns and an unstable internal geometry (Mosbrucker et al., 2017). Irregular distortion can not be fully compensated for by standard camera calibration models, and low internal stability may cause the camera geometry to unintentionally change both within and between surveys. Zoom lenses, like the one used in this study, are especially prone to small changes in focal length that can make the validity of a single camera model questionable. Small differences in focal length are also likely to be caused by using

automatic focusing, and according to Mosbrucker et al. (2017) it might be preferable to treat images taken with a zoom lens or non-fixed focus as being taken by different cameras in the camera calibration process. The exact influence of uncorrected lens distortion on reprojection errors, and ultimately on georeferenced precision and accuracy, in this study is unclear. However, due to the camera setup and the use of a fixed calibration model, both lens irregularities and differences in internal camera geometry between surveys are probable and potentially major sources of uncertainty.

Reprojection errors are also largely affected by the quality of image observations. How precise a surface feature can be detected and distinguished from its immediate surroundings, in several images with different viewing angles, is obviously crucial for the uncertainty related to the resulting tie point's position in the photogrammetric network. This precision is determined by the contrasting features available, given by the surface characteristics and illumination, and the camera setup's ability to capture these features.

Comparing distributions of reprojection errors (figure 4.13) to corresponding survey orthophotos (figure 4.1), low tie point density and high reprojection errors are mainly found in areas with shadow or little surface texture. Tie points are for example lacking in large areas with shadow in Tyinstølen 100219. In the following survey, from the morning after, clouds came in and caused flat light during the last part of the survey, giving reduced tie point density towards the eastern margin of the survey area. The areas with the least detectable surface features, typically areas with newly deposited dry snow, are in all surveys connected to lower tie point density, naturally, and higher reprojection errors. In general, variations in snow surface characteristics and illumination seem to explain most of the variation in reprojection errors within each survey. As a result, lowering the overall reprojection error by further filtering of tie points with high error, would at the same time increase the areas with sparse or no tie point coverage.

Although issues related to surface contrasts and illumination also depend on camera settings such as exposure, standard optical cameras have limited capability of handling the relative difference between bright and dark areas, or a lack of directed and contrasting light, on highly reflecting snow surfaces. Focus, distortion and image blur are on the other hand entirely determined by camera properties and photographing technique. Image sharpness, as a result of focusing, seems relatively equal among the processed surveys. The variations in range during the surveys are not expected to have had any influence on sharpness, as the hyperfocal length for the lens used (a few meters) is exceeded and the focus could as well have been fixed at infinity (Mosbrucker et al., 2017). Lens distortion has probably affected the quality of image observations, by making features appear deformed (see figure 4.4) when situated in areas with large distortion - mainly towards the image edges.

More important, however, is probably the effects of motion blur. As seen by the washed out target colors in figure 4.4, significant blur is present in the imagery and might explain some of the variation in reprojection error between images and surveys. Blur can be caused by camera motion during the sensor exposure time, where motion is mainly controlled by the flying speed of the UAV, vibrations and displacements caused by wind gusts. Recorded exposure times of 1/1000 s and flying speed of 8 m/s mean a maximum camera displacement of 8 mm during single exposures caused by the planned camera motion. This displacement represents roughly one third of a pixel at the obtained ground resolutions and is

not nearly enough to cause the observed blur. Since the most pronounced blur seems to be caused by motion in one direction, sudden changes in the airflow around the UAV seems to be a likely explanation.

While reprojection errors represent the uncertainty of the whole photogrammetric network, tie point precisions show what implications this uncertainty actually have for surface geometry and final DEM precision. The spatial patterns of tie point precisions (figure 4.16 and appendix C) appear similar to those of reprojection errors, and the issues discussed above are also relevant for explaining variations in tie point precision. However, the relation between reprojection errors and tie point precisions is not straight forward. For example are reprojection errors generally decreasing towards the margins, while tie point precision magnitudes generally increase. And both for vertical and horizontal tie point precisions the local variation seems to be larger than for reprojection errors. Key aspects in this regard is how many images each tie point is observed in, and where these images are taken from. Observations from a narrow range of angles make tie point positioning, especially in the viewing direction, very sensitive to image observation errors. Few observations may then result in very uncertain tie point position estimates without this effect being reflected in the associated reprojection errors.

Few observations and low angles of ray convergence might also explain why tie point precision is generally lower in vertical than horizontal direction, since images are taken normal to an average slope that is closer to horizontal than vertical (around 30°). This implies that the lowest tie point precision might be found in the slope normal direction, which unfortunately is the direction of main interest in measurements of snow surface change. Tie point covariances have just recently been made available in the Metashape software, and precision is not yet commonly reported in SfM-based studies. James, Robson and Smith (2017) calculated precision maps based on a Monte Carlo analysis combined with a former version of Metashape (then PhotoScan), and obtained mean precisions of less than 2 cm in horizontal directions and less than 3 cm vertically. Compared to this, the horizontal precisions in this study seem reasonably good, while the vertical precisions are significantly lower. Accounting for possibly lower tie point precisions normal and parallel to the mean slope, the overall photogrammetric precision level seems sub-optimal and raises some questions regarding the reliability and reproducibility of obtained surface geometries.

5.1.2 Georeferencing precision

The georeferencing part of the photogrammetric processing consisted of two components: inclusion and weighting of GCPs in the bundle adjustment, and fitting of the surface geometry to the GCPs ground coordinates. While the first affects the surface shape itself, the latter determine its scale and position in the external coordinate system. As described by James, Robson, d'Oleire Oltmanns and Niethammer (2017), the need for including GCPs in bundle adjustment to obtain an accurate DEM shape depends on the quality of the image geometry and image observations. If the photogrammetric network is strong and can be precisely self-calibrated, less GCPs are needed and their main purpose is to define the datum. On the other hand, if the photogrammetric precision is low and systematic errors likely, a dense network of GCPs can be used to correct and improve surface geometry. In both cases, appropriate weighting of GCPs is required to avoid forcing high accuracy at

GCPs at the expense of overall accuracy.

Errors on GCPs were reduced by one order of magnitude (see table 4.5) by including GCPs in bundle adjustments, showing that the inclusion largely affected surface shapes. GCP and CP errors of generally equal magnitudes indicate that the change in surface shape greatly improved georeferenced accuracy in the region covered by control points. High vertical errors on CPs compared to GCPs in the Tyinstølen 110219 survey indicate, however, that the surface shape in this case is overfitted to GCPs. This is supported by the much lower sensitivity to changes in GCP configuration found for this survey in the GCP analysis (section 4.2.3). The errors on CPs are however not larger than in the other surveys, so the consequences of the overfitting seem minor. As suggested in section 4.2.3, one possible cause might be higher concentration of tie points in the area covered by GCPs. If so, this indicates that careful evaluation of the marker accuracy settings, i.e. the weighting of GCPs versus tie points, for each individual survey could have been beneficial. The importance of correct weighting is also confirmed by the general impact implementing GCPs had on surface shape.

The GCP analysis also shows that the GCP configuration in the Tyinstølen surveys may lead to uncertainty regarding the scaling, orientation and translation of the surface shapes. The GCP analysis was not designed to explicitly quantify this uncertainty, but the results show that small changes in the GCP setup could produce errors exceeding the measured georeferenced accuracy in parts of the survey area. Whether using all 8 GCPs give the most correct result is not certain, but through examination of GCP errors and comparison with the DTM on snow free surfaces, it was confirmed to be a reasonable best guess. This was further verified by DEM comparisons (see section ??), which show no clear signs of large-scale errors related to orientation and scale. Without GCPs in all parts of the survey area, however, the absence of such errors can not be completely ensured.

5.1.3 Systematic errors

As summarised in section 4.3.4, there are clear indications of systematic errors being present in all of the Tyinstølen surveys. The effects comprise both error patterns on GCPs seen across all surveys (figure 4.18), and systematic differences between surveys as seen by comparing the Tyinstølen 150219_1 and 150219_2 DEMs (figure 4.25). DEM shape and errors from the Tyin Lake survey (figure 4.19) give an impression of the potential shape and magnitude of image-scale and model-scale deformations, although the deformations here might be exaggerated due to the very weak geometry of the photogrammetric network. Due to equal camera calibration models and similar flight grids and flying speed, however, it is likely that the DEMs from Tyinstølen suffer from similar deformations. These comprise mainly a slight model-scale bending and elevation shifts along image margins, both increasing in magnitude towards the corners of the surveyed area.

The main causes of these systematic deformations are probably uncorrected lens distortion and poor image geometry, where errors arising from systematic (non-random) distortion is allowed to propagate through the full model. Insufficient camera calibration and the consequences of using a fixed calibration model for photogrammetric precision is already discussed in section 5.1.1. Better image geometry, i.e. more convergent views and changing camera directions (see section 3.2.4.0.2), or controlling surface shape with dense network of GCPs, could have reduced systematic deformations despite uncorrected

distortion in the camera geometry (James, Robson, d'Oleire Oltmanns and Niethammer, 2017).

Another subject that needs to be mentioned in relation to both photogrammetric precision and systematic errors is rolling shutter effects. Rolling shutters are standard among consumer-grade digital cameras today, and is most certainly used in the Mavic 2 Zoom camera as well. Based on other DJI cameras, a likely shutter readout time would be around 30 ms. At a speed of 7-8 m/s, this means the camera probably moves at least 21 cm during the recording of a single image. A vertical line of pixels in the image might in other words represent an oblique line on the ground, with the lower end displaced by 21 cm in the moving direction compared to the upper line. Rolling shutter effects thus represent a potentially major source of reprojection errors as well as systematic errors. Whereas large-scale deformation might have been restricted by alternating flying directions, the distortion in individual images has probably contributed to reduced photogrammetric precision.

During camera calibration, the rolling shutter compensation in the Metashape software was tested and found to significantly reduce reprojection errors. However, it also introduced large-scale deformations in the surface geometry, making the DEM useless in parts distant from GCPs. Because the rolling shutter compensation is calibrated together with the lens distortion parameters, it seems likely that better image geometry is needed to get both parts accurately solved.

5.1.4 Total georeferenced accuracy

In comparison with SfM-MVS survey accuracies commonly reported in geomorphological studies, the relative CP accuracies obtained for the Tyinstølen surveys are high. The ratios between RMSE on CPs and survey range are 2-3 times lower than the median ratio of 1/639 found by Smith and Vericat (2015), and these are in the lower end of ratios found for similar survey ranges. Only a few studies on snow have so far reported the RMSE on independent reference points (points that are not used for model georeferencing). Among these, the vertical RMSEs reported by Avanzi et al. (2017) (0.036-0.069 m) and Harder et al. (2016) (0.085 m), using survey ranges of 60 m and 90 m respectively, are in the same range as the RMSEs on CPs found in this study. Bühler et al. (2017) (0.17-0.23 m) reported higher errors from a survey range of 100 m.

The errors on CPs are, however, only reflecting the accuracy in the part of the survey area that is well covered by GCPs. They are also located on gently inclined and even snow surfaces, where the vertical accuracy is less dependent on horizontal accuracy. Combined with uncertainties related to georeferencing precision and systematic errors, the overall georeferenced accuracies are expected to be lower than what is indicated by errors on CPs. Accuracy is due to the scaling and orientation expected to decrease with distance to the region covered by GCPs, while errors in DEM shape, in addition to distance from GCPs, are expected to be largest towards DEM margins and especially corners. Minimum snow depth observations comparing DEMs to the DTM are all negative and range from -0.1 to -0.37 m for the DEMs without significant noise. Although based on a limited number of snow free surfaces and also involving DTM uncertainty, this might indicate the minimum level of georeferenced accuracy within the survey area.

5.2 Snow depth maps

Calculation of snow depth maps was not part of the main scope of this study. Comparisons of snow surface models with the nationwide, high-resolution LiDAR DTM were however included to demonstrate another practical application of the collected data. The errors on CPs are remarkably low given the uncertainty associated with single probe measurements on variable ground surfaces, and are similar to the errors reported by Harder et al. (2016) and Bühler et al. (2016). These suggest that highly resolved and accurate snow depth measurements can be acquired by only producing a snow surface model wherever the high-resolution DTM is available. This can be useful for e.g. verification of snow cover or snow redistribution models. Detailed snow depth maps are also visually appealing and well suited for education purposes, as mentioned by Deems et al. (2015).

5.3 Snow surface change detection

5.3.1 Methodical considerations

To the author's knowledge, no previous work on snow surface change detection using SfM-MVS or TLS has considered spatially variable DEM uncertainty. Furthermore is statistical significance of DEM differences only found considered by Eker et al. (2018). As stated by James, Robson and Smith (2017), and also supported by the results in this study, an understanding of the uncertainties within DEMs from photogrammetric surveys is necessary to obtain reliable measurements and optimise future surveying. For change detection using SfM-MVS to be part of decision making within the field of natural hazards, these uncertainties also needs to be quantified and integrated in the change analysis.

As a first step, the use of a uniform level of detection (LoD) for DEMs of difference (DoDs) is introduced here. This is a simple method that has some obvious shortcomings. A uniform LoD based on a single accuracy value is first of all only valid in the area in which the accuracy is measured. And within that area, there is a risk that real changes are not detected in areas of high DEM precision and noise is detected as real change in areas of low DEM precision. Only considering vertical accuracy may also result in the LoD being less valid in steep areas, where vertical accuracy is largely affected by horizontal accuracy.

The LoDs were calculated based on the RMSE on CPs only. A more conservative LoD could be obtained by adding a registration error representing the uncertainty in the relative datum measurement between surveys (James, Robson and Smith, 2017). Based on the dGNSS elevation precision this would mean about 2 cm added to the LoDs at a 95 % confidence level. For practical use, $LoD_{95\%}$ between 10 and 20 cm, as obtained here, is in most cases sufficient to reliably detect critical loading in an avalanche release area.

5.3.2 Detected periodical changes

Unfortunately, no build-up of potential avalanche forming slabs was captured in this study. The DEMs of difference, representing snow surface change, demonstrate however at what level of detail and precision patterns of erosion and deposition potentially can be explored and quantified. Below follows a verification of observed snow depth changes (as described

in section 4.5.3) based on the weather observations during the periods (figure 4.22 and 4.23). The terms used for reference to locations within the survey area are explained in figure 4.2.

Period P1 (10th-11th February 2019)

The first period spans almost one day of stably low temperatures, no precipitation and wind from SW to NW gradually picking up to around 10 m/s at the time of the second survey. At the beginning of the period, 5-10 cm of loose, new snow was covering a layer of soft wind-affected snow of 30-50 cm thickness above a thick rain crust. Drifting snow was observed during the second survey, and some erosion and deposition was therefore expected within the survey area.

As described in section 4.5.3, the change seen in the DEM of difference (figure 4.25) seem to represent both photogrammetric errors and real snow depth changes. Significant deposition is found on the southern slope and beneath the cornice on top of the northern slope. This can be well explained by drifting snow with the measured wind speed and direction. Differences below the LoD do also show realistic changes, such as erosion along the ridge and deposition in small depressions and more sheltered regions. The LoD hence seem to be too conservative in parts of the survey area, while at the same time being too low to exclude the noise and the associated propagation of error to nearby regions.

Period P2 (15th February 2019)

This period represent a time span of about 15 minutes. Snow depth change is not likely due to the short time span, no precipitation and low wind speed, in addition to a moist to wet snow surface caused by warm temperatures and previous rain. All change in the DEM of difference (figure 4.25) is therefore caused by errors in one or both of the DEMs, of which the LoD covered most of the change but not all.

Period P3 (11th-15th February 2019)

Period P3 covers a weather episode characterised by several rounds of strong winds from NW, one day of significant snowfall and warm temperatures accompanied by some rain towards the end of the period. A size 2 slab avalanche was observed¹ on the northern slope on the 13th, and was most likely naturally released during the large snowfall with wind speeds exceeding 20 m/s the night before. On the 13th, several size 3 avalanches crossing the road were artificially released on nearby slopes.

The growth of the snowdrift and cornice on top of the northern slope indicates significant deposition of wind-transported snow, which is very likely given the precipitation and wind conditions during the first part of the period. An abrupt transition to no significant loading is shown directly downslope of this area, probably representing the fracture line of the mentioned avalanche. The general decrease in snow depth in the lower parts of the survey area can be the result of both wind erosion early in the period and compaction due to rain and increasing temperatures towards the end. It cannot be excluded, however, that differences in scaling and orientation might have contributed to this.

¹<https://www.regobs.no/Registration/181170>

Period P4 (15th February - 19th March 2019)

Although this period contains several episodes of precipitation and strong winds, relatively small amounts of precipitation make the expected snow depth changes smaller than what the time span normally would imply. High temperatures before and in the first part of the period also caused melt-freeze crusts preventing erosion of older snow. Wind measurements show high wind speeds dominantly from SW to NW, while calmer episodes are associated with wind from more northerly or easterly directions.

The main snow depth increase during the period is found in the depression west of the ridge and just outside the survey area. The appearance indicates that this most likely represents wind-deposited snow, although this is not directly explained by the weather observations which show no episodes of strong wind from east or north. This might however be due to local wind flow patterns around the weather station. Maybe the most interesting change during the period is what seems like downslope creep of the cornice and snowdrift on top of the northern slope (can be seen in detail in section profiles in appendix E). Creep and tilting of cornices are explained by e.g. Vogel et al. (2012), and is a constantly ongoing process due to snow viscosity and the act of gravity. The general increase in snow depth seen within the survey area, being largest in depressions and smaller on protruding terrain formations, is also likely during the given period.

6 Conclusions

This study shows the acquisition of high-resolution snow surface models by UAS aerial surveying and SfM-MVS photogrammetric processing. Snow surface DEMs of an avalanche release area were obtained at 10 cm resolution and sub-decimetre accuracy, using a consumer-grade, lightweight UAS for image acquisition and deployment of ground control points (GCPs) for georeferencing. Repeated surveys allowed the assessment of snow depth change during weather episodes by calculation of DEMs of difference. Confidence-based levels of detection (LoDs) were then applied to evaluate the significance of detected changes based on the accuracy of each DEM. Detected changes were then qualitatively evaluated on the basis of weather observations during the given time periods. The results indicate that snow depth changes of 10-20 cm can be reliably detected within avalanche release areas. Errors and uncertainties within the final DEMs demonstrate, however, the importance of appropriate survey design and careful treatment of errors throughout the photogrammetric processing.

Surveys were carried out partly by one person and with all the necessary survey equipment fitting into a single touring backpack. Thus, this approach can be used for slope-scale snow surface mapping in any area that can be safely accessed by foot or skis. Autonomous flying and image acquisition provided efficient surveying at sufficient precision levels, even with a standard GPS receiver onboard the UAS. Following guidelines given by James, Robson, d'Oleire Oltmanns and Niethammer (2017), the accuracy and precision of final DEMs were optimised during the photogrammetric processing. Important elements included in the processing were analyses of camera calibration parameters, the sensitivity of accuracy settings, GCP performance and tie point precisions. The analyses also allowed for a thorough evaluation of final errors and uncertainties regarding the shape, scale and orientation of the DEMs.

DEM precision and accuracy were mainly limited by weak image geometry. This hindered proper self-calibration of camera model parameters, forcing the use of a fixed, sub-optimal camera model across all surveys. Together, weak image geometry and insufficient camera calibration caused increased reprojection errors, reduced tie point precision and systematic deformations of DEM shape. Survey precision in avalanche release areas is also challenged by limited options for placement of GCPs due to safety reasons. The GCP configuration was found to cause some uncertainty in DEM scaling and orientation, and this uncertainty is difficult to avoid or quantify without GCPs or check points (CPs) covering the full survey area. In general, uncertainties related to both DEM shape and orientation grow larger with distance from the area covered by GCPs. Accuracy measured by errors on CPs, which have the same spatial distribution, is therefore likely to be higher than actual DEM accuracy within the full survey area.

Regarding snow surface characteristics and illumination during surveying, the findings of previous studies (summarised in section 2.3) can be confirmed: Even and highly reflect-

ing snow surfaces are challenging to reconstruct based on optical imagery. The reduced density and quality of image observations found in areas with dry, wind-deposited snow, even with favourable illumination, point at one of the major issues that has to be solved for UAS photogrammetry to be useful in operational avalanche hazard assessment. With the purpose of change detection, one way of reducing uncertainty is to implement spatially variable detection levels. A weakness with applying uniform LoDs, both in general and within this study, is the reduced validity if variations in surface precision is high and if DEM accuracy is based on measurements in only parts of the survey area.

Compared to previous work on photogrammetric mapping of snow surfaces, this study represents a step forward in assessment of causes and consequences of photogrammetric uncertainties. Best practice routines for SfM-MVS processing and reporting of errors suggested within geomorphological disciplines were implemented, thus showing an approach that can be used to enhance DEM quality and form a basis for survey improvements. Assessment of uncertainty in the final product, DEMs of difference representing snow depth change, is further demonstrated by the use of uniform levels of detection. However, this is a method with limited capability of representing the spatially variable errors that can be expected within snow surface DEMs, and is therefore one of many aspects that need further consideration.

To make SfM-MVS processing of UAS imagery a valuable tool within operational avalanche hazard assessment, the goal should be to establish standardized, best practice routines ensuring repeatable measurements with the highest possible accuracy and precision. Based on the experiences made from this study, these routines should cover the full process from initial survey planning to reporting of final errors. Future work on this topic is suggested to include:

- Development of flight planning guidelines that ensure both strong image geometry (high overlap and high convergence) and battery-efficient image acquisition
- Testing the influence of flying speed, ground resolution, light spectra (e.g. use of near-infrared imagery), camera settings and image post-processing routines on image observation quality for low-contrast snow surfaces resulting from poor illumination or small-scale surface features
- Testing alternative methods for georeferencing and error assessment to allow surveying of inaccessible areas (e.g. direct georeferencing with RTK UAS, measure error on check points with reflectorless total station)
- Development of a processing and validation workflow that ensures the highest possible DEM accuracy and precision, but also minimizes processing time and computational requirements
- Development of tools for including spatially variable DEM precision in confidence-based change detection
- Evaluation of the application of 2.5D (DEMs of difference) vs 3D (cloud-to-cloud comparison) techniques for change detection in avalanche release areas
- Verification of repeatability (precision) and accuracy through repeated surveys and comparison with TLS or LiDAR DEMs

References

- Agisoft (2018a). Agisoft Metashape User Manual: Professional Edition, Version 1.5. Available at: https://www.agisoft.com/pdf/metashape-pro_1_5_en.pdf [Accessed 02.04.2019]
- Agisoft (2018b). Metashape Python Reference, Release 1.5.0. Available at: https://www.agisoft.com/pdf/metashape_python_api_1_5_0.pdf [Accessed 02.04.2019]
- Avanzi, F., Bianchi, A., Cina, A., de michele, C., Maschio, P., Pagliari, D., Passoni, D., Pinto, L., Piras, M. and Rossi, L. (2017). *Measuring the snowpack depth with Unmanned Aerial System photogrammetry: comparison with manual probing and a 3D laser scanning over a sample plot.*
- Basnet, K., Muste, M., Constantinescu, G., Ho, H. and Xu, H. (2016). Close range photogrammetry for dynamically tracking drifted snow deposition. *Cold Regions Science and Technology* 121, 141–153.
- Birkeland, K. W., van Herwijnen, A., Reuter, B. and Bergfeld, B. (2018). Temporal changes in the mechanical properties of snow related to crack propagation after loading. *Cold Regions Science and Technology* .
- Brasington, J., Langham, J. and Rumsby, B. (2003). Methodological sensitivity of morphometric estimates of coarse fluvial sediment transport. *Geomorphology* 53 (3), 299–316.
- Bühler, Y., Adams, M. S., Bösch, R. and Stoffel, A. (2016). Mapping snow depth in alpine terrain with unmanned aerial systems (UASs): potential and limitations. *The Cryosphere* 10 (3), 1075–1088.
- Bühler, Y., Adams, M. S., Stoffel, A. and Boesch, R. (2017). Photogrammetric reconstruction of homogenous snow surfaces in alpine terrain applying near-infrared UAS imagery. *International Journal of Remote Sensing* 38 (8-10), 3135–3158.
- Bühler, Y., Marty, M., Egli, L., Veitinger, J., Jonas, T., Thee, P. and Ginzler, C. (2015). Snow depth mapping in high-alpine catchments using digital photogrammetry. *The Cryosphere* 9 (1), 229–243.
- Carbonneau, P. E. and Dietrich, J. T. (2017). Cost-effective non-metric photogrammetry from consumer-grade sUAS: implications for direct georeferencing of structure from motion photogrammetry. *Earth Surface Processes and Landforms* 42 (3), 473–486.

-
- Cimoli, E., Marcer, M., Vandecrux, B., Bøggild, C. E., Williams, G. and Simonsen, S. B. (2017). Application of Low-Cost UASs and Digital Photogrammetry for High-Resolution Snow Depth Mapping in the Arctic. *Remote Sensing* 9 (11).
- Clapuyt, F., Vanacker, V. and Van Oost, K. (2016). Reproducibility of UAV-based earth topography reconstructions based on Structure-from-Motion algorithms. *Geomorphology* 260, 4–15.
- Conlan, M. and Gauthier, D. (2016). Using photogrammetry to temporally compare snowpack thicknesses and calculate volumes. *Proceedings of the 2016 International Snow Science Workshop, Breckenridge* pp. 45–50.
- De Michele, C., Avanzi, F., Passoni, D., Barzaghi, R., Pinto, L., Dosso, P., Ghezzi, A., Gianatti, R. and Della Vedova, G. (2016). Using a fixed-wing UAS to map snow depth distribution: an evaluation at peak accumulation. *The Cryosphere* 10 (2), 511–522.
- Deems, J. S., Gadowski, P. J., Vellone, D., Evanczyk, R., LeWinter, A. L., Birkeland, K. W. and Finnegan, D. C. (2015). Mapping starting zone snow depth with a ground-based lidar to assist avalanche control and forecasting. *Cold Regions Science and Technology* 120, 197–204.
- Deems, J. S., Painter, T. H. and Finnegan, D. C. (2013). Lidar measurement of snow depth: a review. *Journal of Glaciology* 59 (215), 467–479.
- DJI (2019). DJI Mavic 2 Zoom/Pro User Manual v1.8. Available at: https://dl.djicdn.com/downloads/Mavic_2/20190124/Mavic_2_Pro_Zoom_User_Manual_v1.8_.pdf
- Dreier, L., Bühler, Y., Ginzler, C. and Bartelt, P. (2016). Comparison of simulated powder snow avalanches with photogrammetric measurements. *Annals of Glaciology* 57 (71), 371–381.
- EAWS (2019a). Avalanche problems. Available at: <https://www.avalanches.org/standards/avalanche-problems/>
- EAWS (2019b). EAWS Matrix. Available at: <https://www.avalanches.org/standards/eaws-matrix/>
- Eberhard, L., Marty, M., Stoffel, A., Kenner, R. and Bühler, Y. (2018). Photogrammetric snow depth mapping: Evaluation of different platforms and sensors. *Proceedings of the 2018 International Snow Science Workshop, Innsbruck* pp. 403–407.
- Eckerstorfer, M., Bühler, Y., Frauenfelder, R. and Malnes, E. (2016). Remote sensing of snow avalanches: Recent advances, potential, and limitations. *Cold Regions Science and Technology* 121, 126–140.
- Eckerstorfer, M., Solbø, S. and Malnes, E. (2015). Using “Structure-from-Motion” Photogrammetry in Mapping Snow Avalanche Debris. *Wiener Schriften zur Geographie und Kartographie* 21, 171–178.

-
- Eker, R., Aydin, A., Bühler, Y. and Stoffel, A. (2018). SfM-based 3D point clouds in determination of snow depth from high-resolution UAS data as alternative methods: Is it possible to use? *Proceedings of the 2018 International Snow Science Workshop, Innsbruck* pp. 398–402.
- Eker, R., Bühler, Y., Schlögl, S., Stoffel, A. and Aydin, A. (2019). Monitoring of Snow Cover Ablation Using Very High Spatial Resolution Remote Sensing Datasets. *Remote Sensing* 11 (6).
- Fernandes, R., Prevost, C., Canisius, F., Leblanc, S. G., Maloley, M., Oakes, S., Holman, K. and Knudby, A. (2018). Monitoring snow depth change across a range of landscapes with ephemeral snowpacks using structure from motion applied to lightweight unmanned aerial vehicle videos. *The Cryosphere* 12 (11), 3535–3550.
- Fierz, C., Armstrong, R. L., Durand, Y., Etchevers, P., Greene, E., McClung, D. M., Nishimura, K., Satyawali, P. K. and Sokratov, S. A. (2009). The international classification for seasonal snow on the ground. UNESCO. Available at: <https://unesdoc.unesco.org/ark:/48223/pf0000186462>
- Fonstad, M. A., Dietrich, J. T., Courville, B. C., Jensen, J. L. and Carbonneau, P. E. (2013). Topographic structure from motion: a new development in photogrammetric measurement. *Earth Surface Processes and Landforms* 38 (4), 421–430.
- Frauenfelder, R., Solheim, A., Isaksen, K., Romstad, B., Dyrørdal, A. V., Ekseth, K. H. H., Harbitz, A., Harbitz, C. B., Haugen, J. E., Hygen, H. O., Haakenstad, H., Jaedicke, C., Jónsson, , Klæboe, R., Ludvigsen, J., Meyer, N. M., Rauken, T., Skaland, R. G., Sverdrup-Thygeson, K., Aaheim, A., Bjordal, H. and Fevang, P. A. (2017). Impacts of extreme weather events on transport infrastructure in Norway. *Nat. Hazards Earth Syst. Sci. Discuss.* 2017, 1–24.
- Förstner, W. and Wrobel, B. P. (2016). *Photogrammetric Computer Vision: Statistics, Geometry, Orientation and Reconstruction*. Vol. 11 of *Geometry and Computing*, Springer International Publishing, Cham.
- Gaume, J., Gast, T., Teran, J., van Herwijnen, A. and Jiang, C. (2018). Dynamic anticrack propagation in snow. *Nature Communications* 9 (1), 3047.
- Gauthier, D., Conlan, M. and Jamieson, B. (2014). Photogrammetry of fracture lines and avalanche terrain: Potential applications to research and hazard mitigation projects. *Proceedings of the 2014 International Snow Science Workshop, Banff* pp. 109–115.
- Harder, P., Schirmer, M., Pomeroy, J. and Helgason, W. (2016). Accuracy of snow depth estimation in mountain and prairie environments by an unmanned aerial vehicle. *The Cryosphere* 10 (6), 2559–2571.
- Håland, G., Orset, K. I., Frekhaug, M. H. and Norem, H. (2015). *Sammenligning av modelleringsverktøy for norske snøskred*. NVE, Oslo. Rapport nr 107-2015.

-
- James, M. R. and Robson, S. (2012). Straightforward reconstruction of 3D surfaces and topography with a camera: Accuracy and geoscience application. *Journal of Geophysical Research: Earth Surface* 117 (F3).
- James, M. R. and Robson, S. (2014). Mitigating systematic error in topographic models derived from UAV and ground-based image networks. *Earth Surface Processes and Landforms* 39 (10), 1413–1420.
- James, M. R., Robson, S., d'Oleire Oltmanns, S. and Niethammer, U. (2017). Optimising UAV topographic surveys processed with structure-from-motion: Ground control quality, quantity and bundle adjustment. *Geomorphology* 280, 51–66.
- James, M. R., Robson, S. and Smith, M. W. (2017). 3-D uncertainty-based topographic change detection with structure-from-motion photogrammetry: precision maps for ground control and directly georeferenced surveys. *Earth Surface Processes and Landforms* 42 (12), 1769–1788.
- Kraus, K. (1993). *Photogrammetry: Fundamentals and standard processes*. Vol. 1, 4th ed., Dümmler, Bonn.
- Kraus, K. (2007). *Photogrammetry: Geometry from images and laser scans*. Walter De Gruyter.
- Lague, D., Brodu, N. and Leroux, J. (2013). Accurate 3D comparison of complex topography with terrestrial laser scanner: Application to the Rangitikei canyon (N-Z). *ISPRS Journal of Photogrammetry and Remote Sensing* 82, 10–26.
- Luhmann, T. (2011). *Close range photogrammetry : principles, techniques and applications*. Whittles Publishing.
- McClung, D. and Schaerer, P. A. (2006). *The avalanche handbook*. Third ed., The Mountaineers Books.
- Milan, D. J., Heritage, G. L., Large, A. R. G. and Fuller, I. C. (2011). Filtering spatial error from DEMs: Implications for morphological change estimation. *Geomorphology* 125 (1), 160–171.
- Mosbrucker, A. R., Major, J. J., Spicer, K. R. and Pitlick, J. (2017). Camera system considerations for geomorphic applications of SfM photogrammetry. *Earth Surface Processes and Landforms* 42 (6), 969–986.
- Mott, R., Schirmer, M., Bavay, M., Grünewald, T. and Lehning, M. (2010). Understanding snow-transport processes shaping the mountain snow-cover. *The Cryosphere* 4 (4), 545–559.
- Müller, K., Mitterer, C., Engeset, R., Ekker, R. and Kosberg, S. (2016). Combining the Conceptual Model of Avalanche Hazard with the Bavarian Matrix. *Proceedings of the 2016 International Snow Science Workshop, Breckenridge* pp. 472–479.

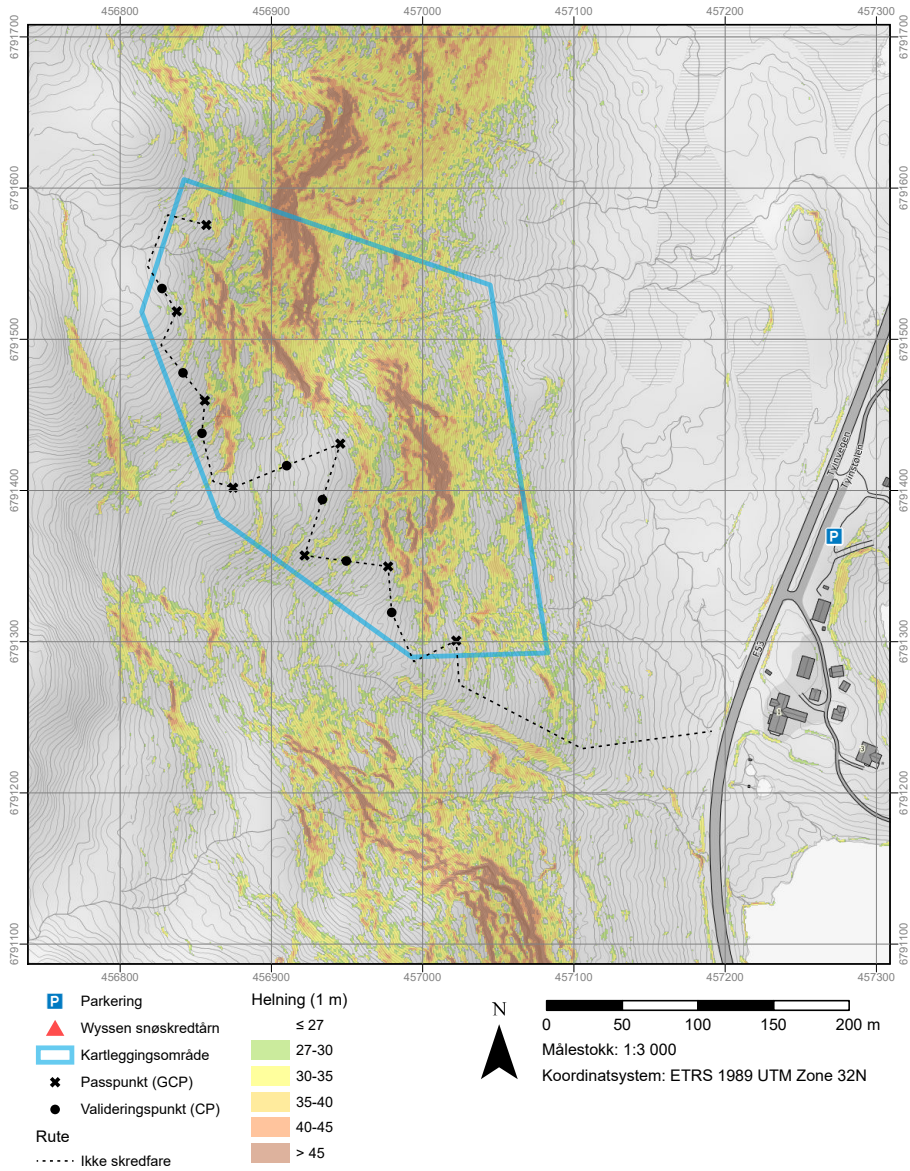
-
- Nolan, M., Larsen, C. and Sturm, M. (2015). Mapping snow depth from manned aircraft on landscape scales at centimeter resolution using structure-from-motion photogrammetry. *The Cryosphere* 9 (4), 1445–1463.
- Norem, H. (1974), Utforming av veger i drivsnømråder, Thesis. Avhandling (tekn. lic.) - Norges tekniske høgskole, 1974.
- Peitzsch, E., Fagre, D., Hendriks, J. and Birkeland, K. (2018). Detecting snow depth change in avalanche path starting zones using uninhabited aerial systems and structure from motion photogrammetry. *Proceedings of the 2018 International Snow Science Workshop, Innsbruck* pp. 408–412.
- Peitzsch, E. H., Hendriks, J. and Fagre, D. B. (2016). Using structure from motion photogrammetry to examine glide snow avalanches. *Proceedings of the 2016 International Snow Science Workshop, Breckenridge* pp. 492–500.
- Pepe, M., Fregonese, L. and Scaioni, M. (2018). Planning airborne photogrammetry and remote-sensing missions with modern platforms and sensors. *European Journal of Remote Sensing* 51 (1), 412–436.
- Pix4D (2019). Reprojection error. Available at:
<https://support.pix4d.com/hc/en-us/articles/202559369-Reprojection-error>
- Prokop, A. (2008). Assessing the applicability of terrestrial laser scanning for spatial snow depth measurements. *Cold Regions Science and Technology* 54 (3), 155–163.
- Prokop, A., Schön, P., Singer, F., Pulfer, G., Naaim, M., Thibert, E. and Soruco, A. (2015). Merging terrestrial laser scanning technology with photogrammetric and total station data for the determination of avalanche modeling parameters. *Cold Regions Science and Technology* 110, 223–230.
- Schweizer, J., Bruce Jamieson, J. and Schneebeili, M. (2003). Snow avalanche formation. *Reviews of Geophysics* 41 (4).
- Schweizer, J., Kronholm, K., Jamieson, J. B. and Birkeland, K. W. (2008). Review of spatial variability of snowpack properties and its importance for avalanche formation. *Cold Regions Science and Technology* 51 (2), 253–272.
- Schön, P., Naaim-Bouvet, F., Vionnet, V. and Prokop, A. (2018). Merging a terrain-based parameter with blowing snow fluxes for assessing snow redistribution in alpine terrain. *Cold Regions Science and Technology* 155, 161–173.
- Smith, F. M., Cooper, C. F. and Chapman, E. G. (1967). Measuring snow depths by aerial photography. *Proceedings of the 35th Annual Western Snow Conference, Boise, Idaho, USA* .
- Smith, M. W., Carrivick, J. L. and Quincey, D. J. (2015). Structure from motion photogrammetry in physical geography. *Progress in Physical Geography: Earth and Environment* 40 (2), 247–275.

-
- Smith, M. W. and Vericat, D. (2015). From experimental plots to experimental landscapes: topography, erosion and deposition in sub-humid badlands from Structure-from-Motion photogrammetry. *Earth Surface Processes and Landforms* 40 (12), 1656–1671.
- Statens kartverk (2019). CPOS. Available at:
<https://www.kartverket.no/posisjonstjenester/cpos/>
- Statham, G., Haegeli, P., Greene, E., Birkeland, K., Israelson, C., Tremper, B., Stethem, C., McMahon, B., White, B. and Kelly, J. (2018). A conceptual model of avalanche hazard. *Natural Hazards* 90 (2), 663–691.
- Tedesco, M. (2015). Remote sensing of the cryosphere. John Wiley Sons, Inc. Includes bibliographical references and index.
- Vander Jagt, B., Lucieer, A., Wallace, L., Turner, D. and Durand, M. (2015). Snow Depth Retrieval with UAS Using Photogrammetric Techniques. *Geosciences* 5 (3).
- Vogel, S., Eckerstorfer, M. and Christiansen, H. H. (2012). Cornice dynamics and meteorological control at Gruvefjellet, Central Svalbard. *The Cryosphere* 6 (1), 157–171.
- Westoby, M. J., Brasington, J., Glasser, N. F., Hambrey, M. J. and Reynolds, J. M. (2012). ‘Structure-from-Motion’ photogrammetry: A low-cost, effective tool for geoscience applications. *Geomorphology* 179, 300–314.
- Wheaton, J. M., Brasington, J., Darby, S. E. and Sear, D. A. (2010). Accounting for uncertainty in DEMs from repeat topographic surveys: improved sediment budgets. *Earth Surface Processes and Landforms* 35 (2), 136–156.

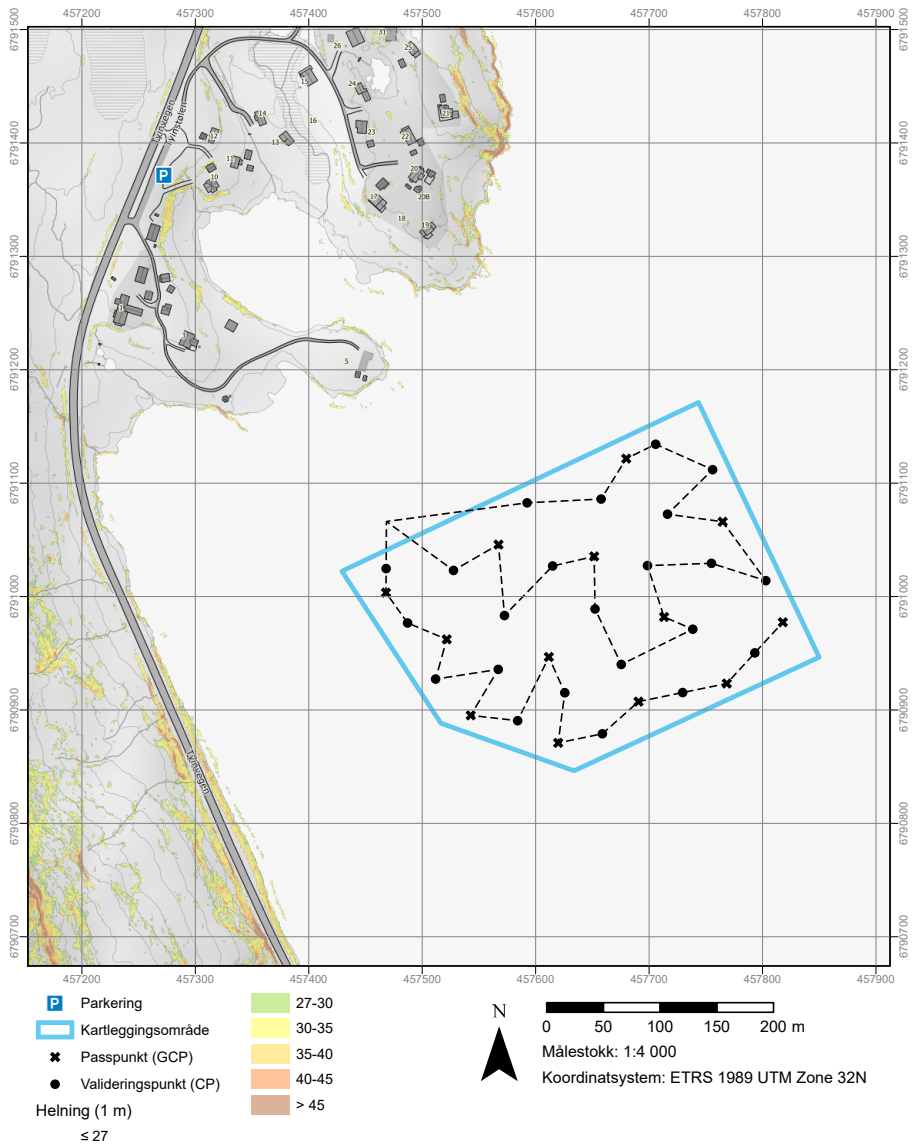
Appendices

A Survey and safety plans (turplaner)

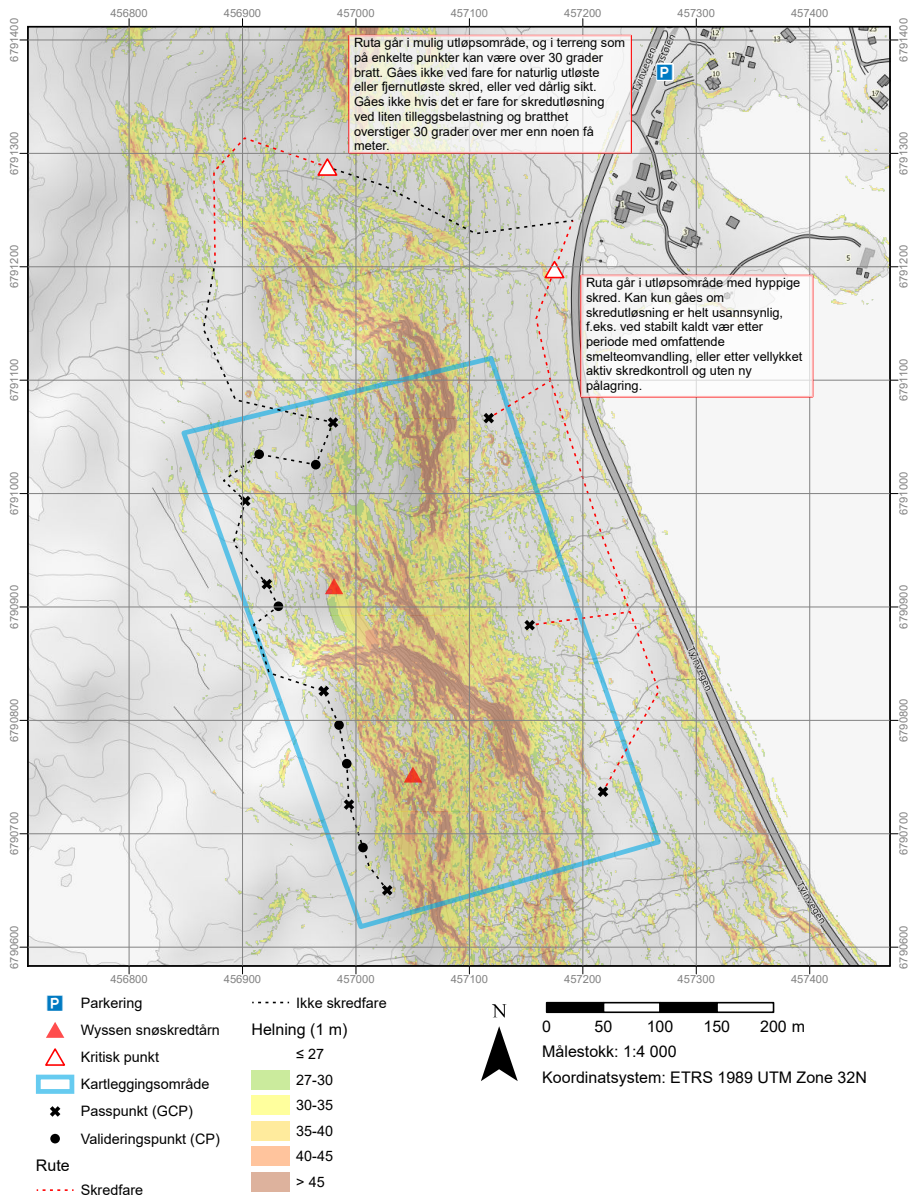
Turplan: Tyinstølen



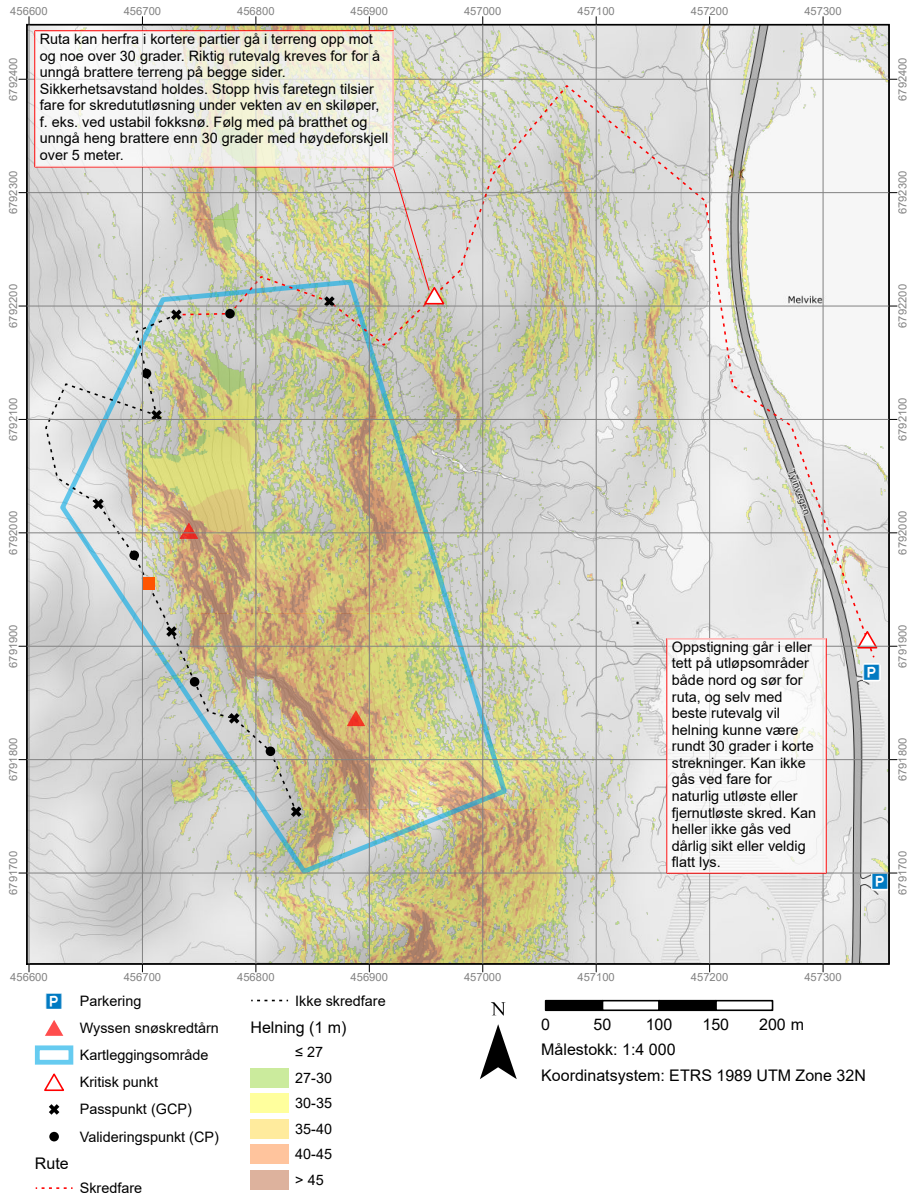
Turplan: Tyn



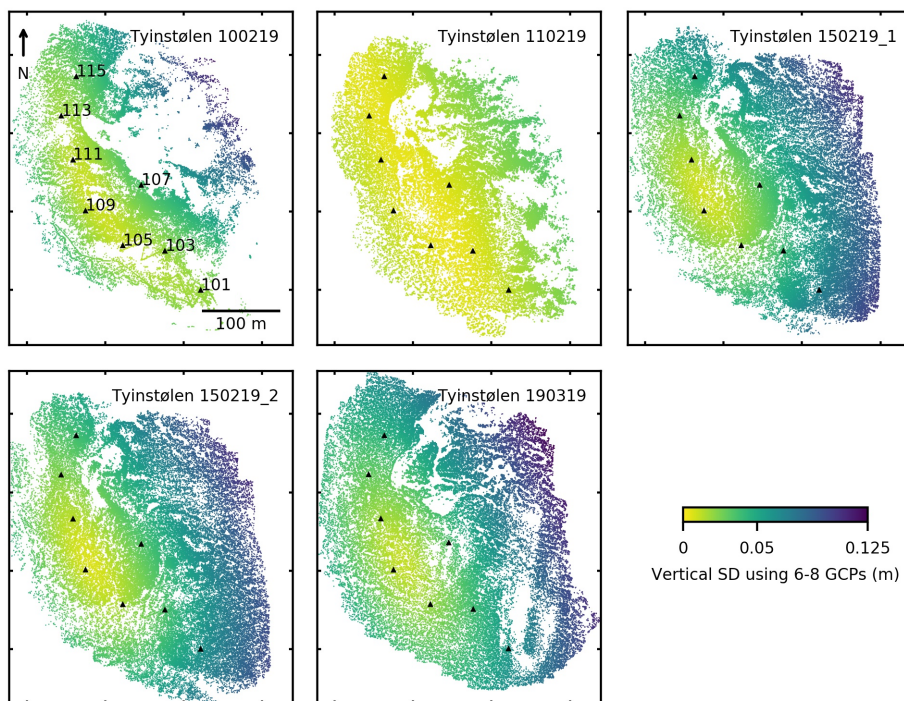
Turplan: Støl



Turplan: Melvike

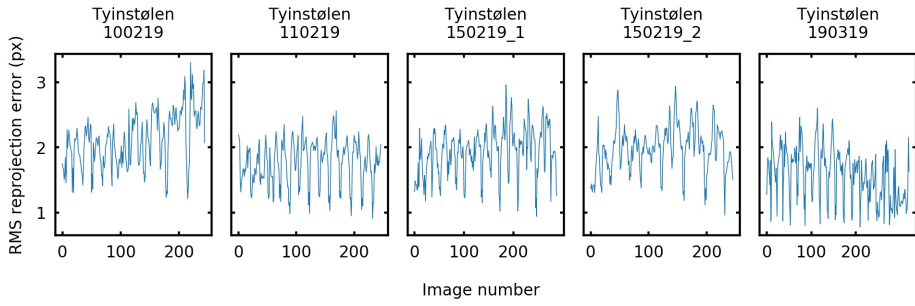


B GCP analysis

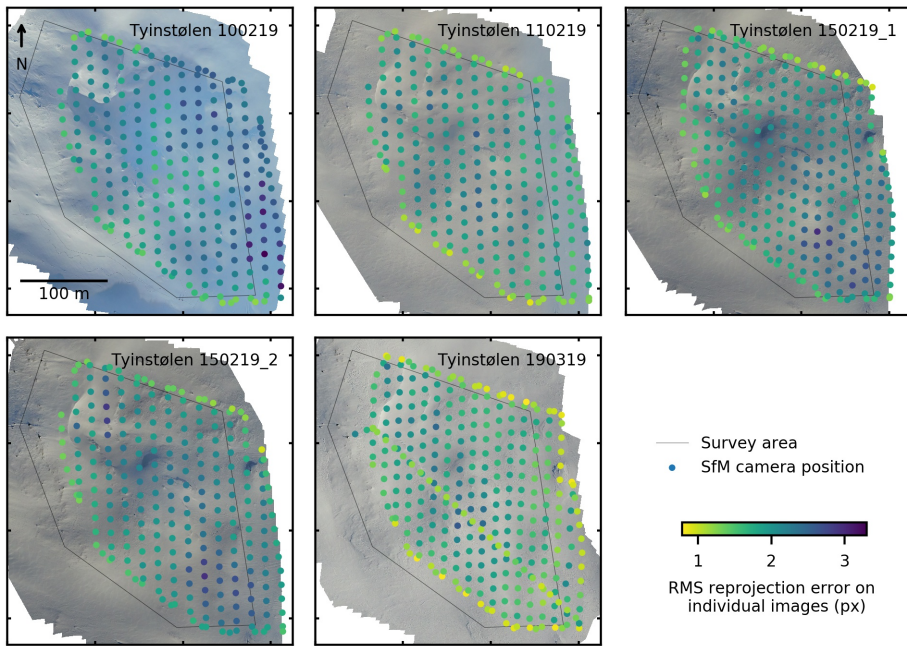


Horizontal variations of tie point positions for all possible configurations of 6-8 enabled GCPs ($n=37$), shown by the standard deviation on each point. Black symbols show GCP locations.

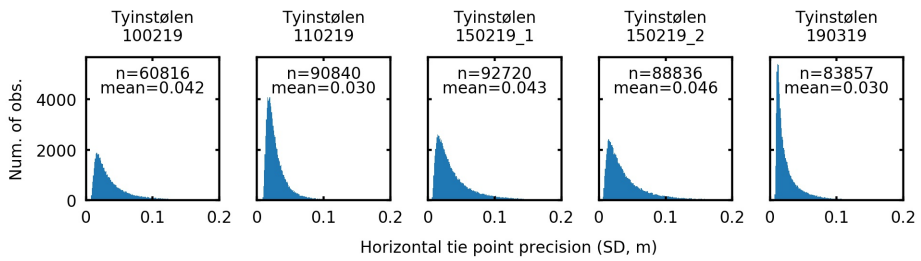
C Photogrammetric precision



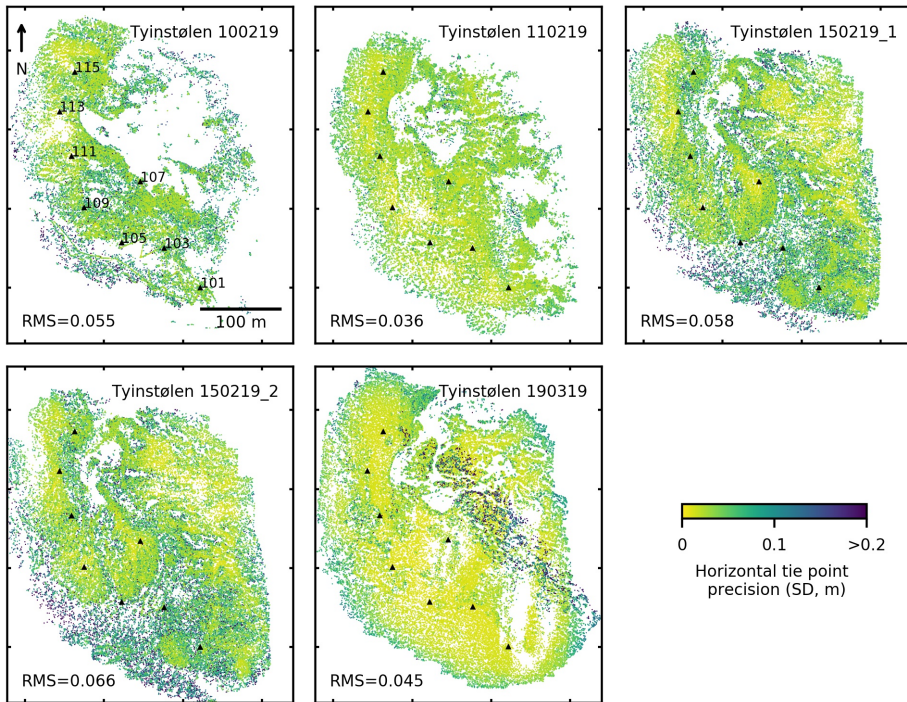
Reprojection errors on individual images.



Reprojection errors on individual images, spatial distribution by estimated camera positions.

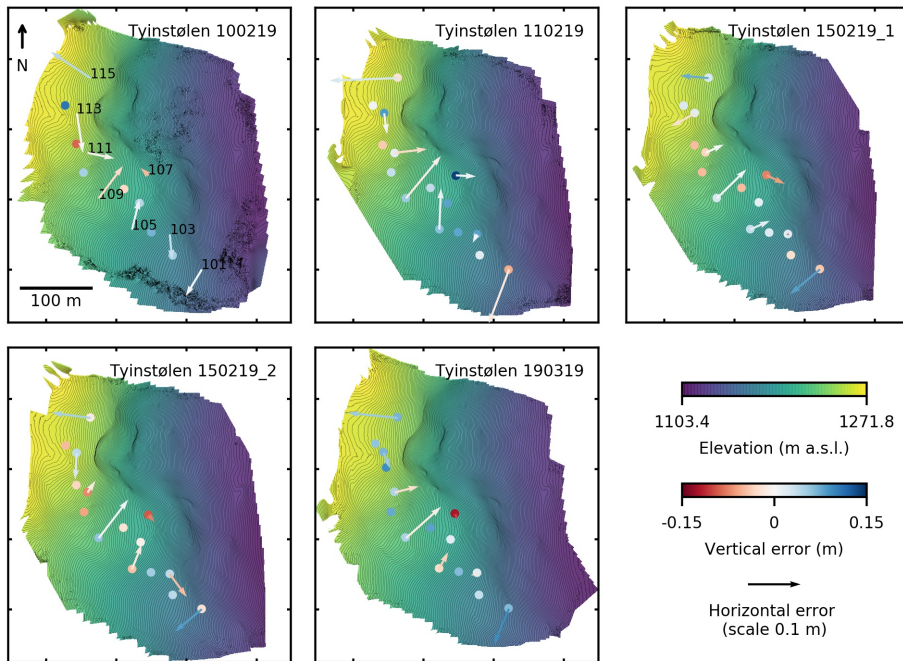


Spatial distribution of horizontal tie point precisions.



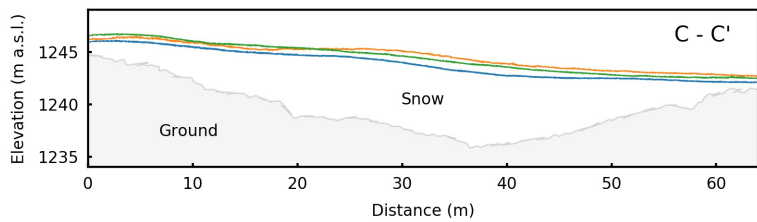
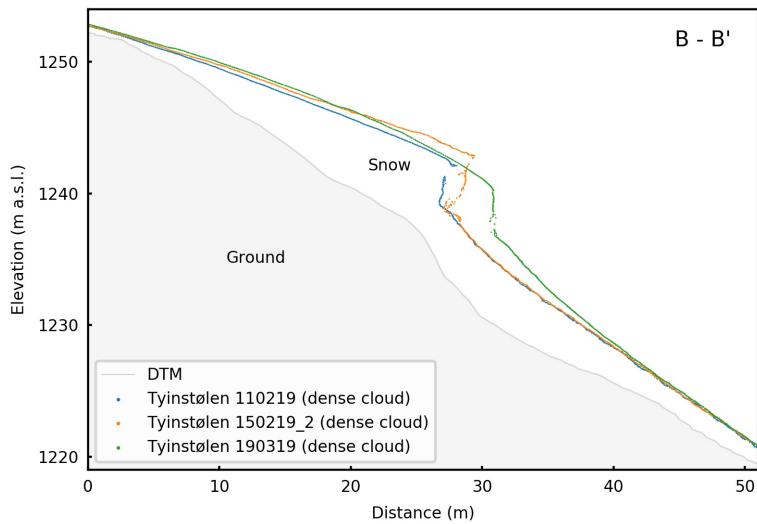
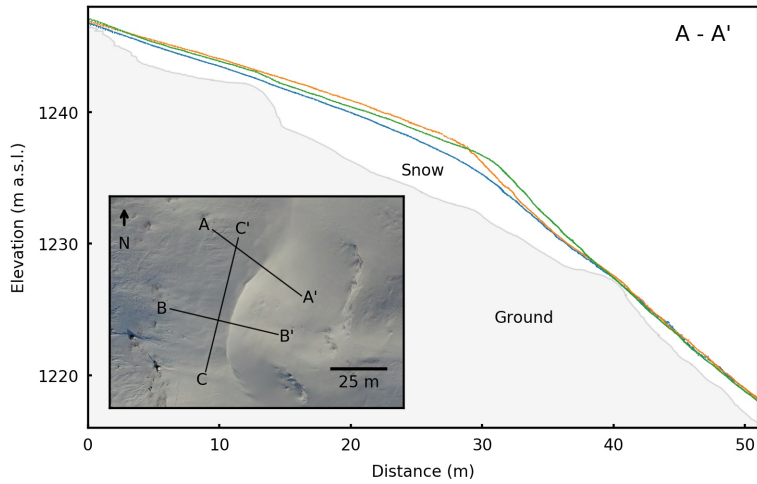
Spatial distribution of horizontal tie point precisions.

D Georeferencing errors



Spatial distribution of errors on GCPs and CPs shown on 0.10 m resolution DEMs with 1 m contourlines. Colored arrows represent GCP errors, where the vertical error component is shown by the color and the horizontal component by the arrow length and direction. Colored dots show the vertical errors on CPs.

E Section profiles



Section profiles, or more precisely section clouds, from dense point clouds and the DTM. Points were extracted using the 'Extract section' tool in CloudCompare with section widths of 0.25 m.